The importance of wind and buoyancy forcing for the boundary density variations and the geostrophic component of the AMOC at 26°N

The Importance of Wind and Buoyancy Forcing for the Boundary Density Variations and the Geostrophic Component of the AMOC at 26°N

IRENE POLO, JON ROBSON, AND ROWAN SUTTON

NCAS-Climate, Department of Meteorology, University of Reading, Reading, United Kingdom

MAGDALENA ALONSO BALMASEDA

European Centre for Medium-Range Weather Forecasts, Reading, United Kingdom

(Manuscript received 4 December 2013, in final form 22 May 2014)

ABSTRACT

It is widely thought that changes in both the surface buoyancy fluxes and wind stress drive variability in the Atlantic meridional overturning circulation (AMOC), but that they drive variability on different time scales. For example, wind forcing dominates short-term variability through its effects on Ekman currents and coastal upwelling, whereas buoyancy forcing is important for longer time scales (multiannual and decadal). However, the role of the wind forcing on multiannual to decadal time scales is less clear. Here the authors present an analysis of simulations with the Nucleus for European Modelling of the Ocean (NEMO) ocean model with the aim of explaining the important drivers of the zonal density gradient at 26°N, which is directly related to the AMOC. In the experiments, only one of either the wind stress or the buoyancy forcing is allowed to vary in time, whereas the other remains at its seasonally varying climatology. On subannual time scales, variations in the density gradient, and in the AMOC minus Ekman, are driven largely by local wind-forced coastal upwelling at both the western and eastern boundaries. On decadal time scales, buoyancy forcing related to the North Atlantic Oscillation dominates variability in the AMOC. Interestingly, however, it is found that wind forcing also plays a role at longer time scales, primarily impacting the interannual variability through the excitation of Rossby waves in the central Atlantic, which propagate westward to interact with the western boundary, but also by modulating the decadal time-scale response to buoyancy forcing.

1. Introduction

The Atlantic meridional overturning circulation (AMOC) is a key component of the Earth's climate. It comprises a northward flow of warm water in the upper 1 km, overlaying a southward flow of cold and denser water (Cunningham and Marsh 2010). Given its large northward heat transport, it is thought that variations in the strength of the AMOC play an essential role in modulating the climate (Knight et al. 2005; Sutton and Hodson 2007; Robson et al. 2012, 2013; Sutton and Dong 2012). Because of this potentially large impact on climate, there is a significant interest in predicting the AMOC's evolution over the next decade (Meehl et al. 2009; Matei et al. 2012; Pohlmann et al. 2013). To be able to understand the potential predictability of the AMOC, to properly attribute its role in climate, and to help initialize the potentially predictable components of the AMOC in future prediction systems, it is important to understand the mechanisms that govern the strength of the AMOC.

Thanks to the Rapid Climate Change (RAPID) program, the AMOC has been observed continuously at 26.5°N since 2004 (Cunningham et al. 2007). The observing system is based on a transbasin array of moored instruments, which measures the basinwide strength and vertical structure of the AMOC and its components (Cunningham et al. 2007). In particular, full-depth moorings are deployed to measure temperature and salinity at the two margins of the Atlantic. These

Denotes Open Access content.

Corresponding author address: Irene Polo, NCAS-Climate, Department of Meteorology, University of Reading, Early Gate, RG 66 BB, Reading, United Kingdom.
E-mail: i.polo@reading.ac.uk

DOI: 10.1175/JPO-D-13-0264.1

observations provide an unprecedented opportunity to understand the variability of the AMOC and provide the motivation for our study to investigate the mechanisms that govern variability in density at the eastern and western boundaries of the Atlantic Ocean and hence in the AMOC. Given the large interannual variability observed recently (McCarthy et al. 2012), a particular focus is to understand the processes that are responsible for variability on different time scales.

At short time scales (months to seasonal) it is well understood that changes in the momentum forcing can change the strength of the AMOC. For example, it is well known that changes in the zonal wind stress can change the meridional Ekman currents (Jayne and Marotzke 2001; Hirschi et al. 2003, 2007). Alongshore winds are also likely to project onto the AMOC (Köhl 2005), and local wind stress curl anomalies near the eastern boundary of the Atlantic basin also contribute to seasonal variations of the strength of the AMOC at 26°N by heaving the isopycnals up and down (Kanzow et al. 2010).

At decadal time scales, it is generally thought that variations in surface buoyancy fluxes dominate the variability of the AMOC by driving density anomalies in the deep North Atlantic. Model studies have shown that the density anomalies propagate southward by advection (Marotzke and Klinger 2000), oceanic waves (Kawase 1987; Johnson and Marshall 2002; Hodson and Sutton 2012), or both (Zhang 2010) and affect the strength of the AMOC as they do so. Studies of different long-coupled general circulation model (GCM) simulations have suggested that the North Atlantic Oscillation (NAO) is the main trigger for the variations in deep convection in the Labrador and Greenland–Iceland–Norwegian (GIN) Seas, which eventually drive AMOC variations on decadal time scales (Timmermann et al. 1998; Grötzner et al. 1998; Delworth and Greatbatch 2000; Eden and Jung 2001; Eden and Willebrand 2001; Haak et al. 2003; Bentsen et al. 2004; Dong and Sutton 2005; Böning et al. 2006; Persechino et al. 2012; Robson et al. 2012; Stepanov and Haines 2013). The overall conclusion of the above-mentioned works is that subpolar westerly (easterly) winds associated with positive (negative) NAO-phase force changes in density through an increase (reduction) in surface heat loss over the Labrador Sea and an increase (reduction) in Ekman upwelling in the subpolar gyre. The ocean adjustment, including the Rossby wave adjustment in the interior, takes several years to complete the cycle (Johnson and Marshall 2002). Therefore, it has been found that some of the predictability for the AMOC at 26°N comes from air–sea fluxes over the Labrador Sea and density anomalies south of the Greenland–Scotland Ridge leading by several years (Ortega et al. 2011).

Other works have pointed out the response of the gyre circulation to local wind stress curl anomalies associated with the NAO (Dong and Sutton 2001; Eden and Willebrand 2001). For instance, Eden and Willebrand (2001) argued that a positive (negative) NAO phase excites a fast response involving an anticyclonic (cyclonic) circulation occurring in the region of Subpolar Front due to Sverdrup balance, which changes the ocean heat transport in the basin. Another interpretation of this NAO-driven circulation was described by Marshall et al. (2001) as an "intergyre gyre." Latitudinal variations in the Gulf Stream path due to atmospheric variations are suggested to be related to AMOC variability at interannual to decadal time scales in the observations (Frankignoul et al. 2001) and in oceanic models (de Coëtlogon et al. 2006; Zhang 2008). The in-phase relationship between variation in the AMOC and the Gulf Stream is consistent with the idea that the NAO pattern contributes to both wind-driven and buoyancy-driven circulations on similar time scales (de Coëtlogon et al. 2006).

The AMOC may also be partitioned into geostrophic and ageostrophic components. The ageostrophic component is mainly due to the aforementioned Ekman transports (Lee and Marotzke 1998; Hirschi et al. 2003; Hirschi and Marotzke 2007; Baehr et al. 2004). The geostrophic part of the AMOC is the largest contribution and can be defined from the thermal wind balance in which the geostrophic shear is calculated from the zonal density gradients (Marotzke et al. 1999). Using numerical models, some authors have shown that AMOC variability can be largely reproduced from the knowledge of boundary densities and zonal wind stress (Hirschi and Marotzke 2007; Baehr et al. 2004). There is also consensus that high-frequency variability (<3 yr) in the AMOC is related to variations in the Ekman component (ageostrophic), while multiannual variations are associated with the geostrophic transports (Sime et al. 2006; Hirschi and Marotzke 2007; Hirschi et al. 2007; Cabanes et al. 2008; Balan-Sarojini et al. 2011; Hodson and Sutton 2012).

Although it is well established that the buoyancy forcing is an important source of variability of the geostrophic transports, it has been suggested that wind forcing can potentially influence density locally at the Atlantic margins, thus modulating the zonal density gradient and the AMOC (Hirschi et al. 2007; Hodson and Sutton 2012). For instance, Köhl (2005) found that the heaving of isopycnals due to wind forcing near the eastern boundary can explain ~70% of the wind-driven variations of the AMOC at seasonal time scales. Density anomalies generated at the eastern basin could propagate westward and influence AMOC variability at interannual time scales. However, the author only

analyzed 10 yr of data; therefore, mechanisms that drive interannual and slower changes in AMOC could not be well captured by his analysis. Also, using 11-yr integrations, Cabanes et al. (2008) have shown with OGCM sensitivity experiments how interannual variations of the wind stress curl in the western Atlantic account for much of the variability in pycnocline depth and thus in the strength of the AMOC at 28°N. Finally, Biastoch et al. (2008) have unraveled the characteristics of midlatitude AMOC variability related to heat fluxes and wind variability separately. Interestingly, they found that the wind appears to explain part of the variability of meridional transports at interannual and decadal time scales; however, the mechanisms behind the wind-driven AMOC variability at these time scales are not fully explained.

This study aims to further understand the important mechanisms that drive changes in the strength of the AMOC at 26°N and their relationship to wind (momentum) and buoyancy forcing. We will also focus on the relative importance of the mechanisms on different time scales. We will build on previous work by investigating the importance of wind and buoyancy forcings separately by only allowing one to vary at a time. Thus, we will identify the fingerprint of wind and buoyancy forcing on the zonal density gradients, and hence variability of the AMOC, at 26°N. For the different forcings and time scales, we will answer the following questions: (i) How does the zonal density gradient vary at 26°N? (ii) How does the density variability relate to AMOC variability at 26°N? (iii) What are the mechanisms related to the density variability?

The paper is divided as follows: The model simulations and the methodology are described in section 2. The results section (section 3) first describes the different time scales associated with each forcing (section 3a) before the density variability at 26°N is analyzed in section 3b. Section 3c is devoted to understanding the processes that govern the response of the geostrophic AMOC variability to wind and buoyancy forcing separately, and section 4 discusses the combined response to wind and buoyancy forcing, including interactions. Conclusions are presented in section 5.

2. Methodology

a. The model and the experiments

A set of multidecadal ocean-only simulations have been conducted by forcing an ocean model with atmospheric forcing fluxes. The model version and forcing fluxes are those used for the European Centre for Medium-Range Weather Forecasts (ECMWF) Ocean Reanalysis System, version 4 (ORAS4), ocean reanalysis (Balmaseda et al. 2013), but these experiments are performed without any data assimilation. The model is based on the Nucleus for European Modelling of the Ocean (NEMO V3.0; Madec et al. 1998) that is a primitive equation z-level model making use of the hydrostatic and Boussinesq approximations. The model employs a free surface (Roullet and Madec 2000) with partial cell topography (Adcroft et al. 1997). The version used has a tripolar ORCA grid, global configuration with $1° \times 1°$ horizontal resolution, and a tropical refinement to $1/3°$ (ORCA1). The model has 42 vertical levels with thicknesses ranging from 10 m at the surface to 250 m at the ocean bottom. The configuration employs an energy–enstrophy conserving momentum advection scheme (Barnier et al. 2006) and a Laplacian diffusion. Horizontal viscosity is parameterized with a Laplacian operator. Additionally, the ORCA1 configuration makes use of the Gent and McWilliams (1990) mixing parameterization. Vertical mixing is parameterized using a one-equation turbulent kinetic energy scheme (Blanke and Delecluse 1993). More details may be found in Barnier et al. (2006) and Penduff et al. (2007).

Initial conditions are taken from the second iteration of a 50-yr cyclic model spinup, each cycle spanning the period 1958–2008. The OGCM is forced with atmospheric daily fluxes as boundary conditions taken from the 40-yr ECMWF Re-Analysis (ERA-40; Uppala et al. 2005) and the Interim ECMWF Re-Analysis (ERA-Interim; Dee et al. 2011) for the periods 1958–88 and 1989–2010, respectively. Although these are two different datasets, no significant difference between the use of ERA-40 and ERA-Interim was found in the ORAS4 reanalysis for the period 1989–2002 (Balmaseda and Mogensen 2010). The control experiment (hereinafter CTRL) is forced with time-varying daily surface fluxes, heat fluxes, freshwater fluxes (buoyancy forcing), and momentum fluxes (wind forcing) for the time period 1958–2010. The sea surface temperature (SST) is weakly relaxed to daily varying values with a relaxation time scale of about 1 month, while the sea surface salinity (SSS) is restored to climatological SSS with a time scale of 1 yr. There is no ice model, instead the observed sea ice concentration is used to correct the model SST; wherever the sea ice concentration in the observations exceeds 55%, the model SSTs are nudged more strongly (1-day time scale) to the freezing point (−1.8°C). The restoration to SSS and SST is stronger under sea ice (30 days and 1 day, respectively) in order to simulate the buoyancy forcing associated with the melting and creation of sea ice.

A useful way to separate between mechanisms that are due to different forcings is to separate the wind and buoyancy forcings (Biastoch et al. 2008; Robson et al.

2012; Yeager and Danabasoglu 2014). Therefore, two additional experiments are conducted in which only one forcing (either wind or buoyancy) is allowed to vary with time; the other is held at its seasonal-varying daily climatology. Thus, in the experiment referred to as BUOY, the momentum flux is from the ERA-Interim 1989–2010 climatology, while the buoyancy forcing (heat, freshwater flux, and SST) is still time varying. In the experiment referred to as WIND, the momentum flux is time varying, but the buoyancy forcing is from a daily climatology. Model outputs are monthly means.

b. *The meridional overturning circulation in the model*

Previous works have shown that the model used here is a useful tool for understanding the AMOC variability (i.e., Stepanov and Haines 2013). The AMOC at 26°N in the control experiment shows comparable amplitude variability, although the mean AMOC is weaker [~5 Sverdrups (Sv; 1 Sv $\equiv 10^6\,\mathrm{m^3\,s^{-1}}$) difference at 1000 m] than that observed by the RAPID array (Roberts et al. 2013).

Time series of the AMOC are defined as the overturning streamfunction at 26°N and at 1160-m depth [the level of the mean maximum transport at 26°N in the model but also in the observations, i.e., Kanzow et al. (2010)], which will be used as a reference level for the three experiments. We have defined the geostrophic component of the AMOC after subtracting the Ekman component from the total AMOC index (Fig. 1).

The total overturning streamfunction is calculated following Eq. (1):

$$\psi(y,z,t) = \int_{-h}^{z}\int_{x_W(y,z)}^{x_E(y,z)} v(x,y,z,t)\,dx\,dz, \qquad (1)$$

where v is the full meridional velocity component, and it is integrated from the western (x_W) to eastern (x_E) limits of the basin and from a bottom ($-h$) to a particular depth z, where $-h \le z \le 0$. The Ekman component can be obtained from the wind field (Gill 1982). We have calculated the Ekman component from ERA reanalysis surface winds following Baehr et al. (2004) and Hirschi and Marotzke (2007) and Eq. (2):

$$v_{\mathrm{ek}}(y,t) = -\frac{1}{\rho_0 f A_d}\int_0^{L(y)} \tau_x(x,y,t)\,dx. \qquad (2)$$

The term τ_x is the zonal wind stress. The value A_d is the cross section of the Ekman layer, where d denotes the surface Ekman layer depth in which the transport is confined. We have chosen a typical value of $d = 50$ m. The quantity ρ_0 is a reference density, f is the Coriolis parameter, and L is the zonal basin width. The Ekman transport is assumed to be compensated by a barotropic return flow (Jayne and Marotzke 2001; Hirschi and Marotzke 2007):

$$v_{\mathrm{ekc}}(y,t) = \begin{cases} v_{\mathrm{ek}}\left(1 - \dfrac{A_d}{A}\right) & \text{if} \quad -d > z \\ -v_{\mathrm{ek}}\left(-\dfrac{A_d}{A}\right) & \text{if} \quad -d < z \end{cases}. \qquad (3)$$

The variable v_{ekc} represents the meridional velocity due to Ekman and corrected by the compensated return flow. The term A is the total Atlantic cross section. The geostrophic transport anomalies are therefore calculated as

$$\psi'_{\mathrm{geo}}(y,z,t) = \int_{-h}^{z}\int_{x_W}^{x_E} v'(x,y,z,t)\,dx\,dz - \int_{-h}^{z}\int_{x_W}^{x_E} v'_{\mathrm{ekc}}(x,y,z,t)\,dx\,dz. \qquad (4)$$

The baroclinic part can also be expressed as the thermal wind formula (Marotzke et al. 1999):

$$v_{\mathrm{tw}} = \frac{g}{\rho_0 f}\int_{-h}^{z}\frac{1}{L}(\rho_W - \rho_E)\,dz. \qquad (5)$$

The terms ρ_W and ρ_E are the densities' values at the western and eastern side of the Atlantic basin, respectively, and g is the gravity acceleration. We have found that the geostrophic transports' anomalies calculated following Eq. (4) and calculated from thermal wind balance [Eq. (5)] show large similarities in the amplitude and its variability (not shown), therefore suggesting that the baroclinic part is dominant. However, we recognize that barotropic variability may also be present (Sime et al. 2006).

The time series of the geostrophic AMOC index (hereinafter referred to as the AMOC index) has been standardized and filtered with a Parzen filter, following the methodology of Hirschi et al. (2007), after removing the seasonal cycle and the linear trend. The other variables used in the study (density, surface winds, Ekman pumping, and sea level pressure) have also been filtered after removing the seasonal cycle and the linear trend. The Parzen filter is a low-pass, Gaussian-like windowed filter. The following equation defines the N-point Parzen window (Parzen 1962; Harris 1978) over the interval $-[(N-1)/2] \le n \le [(N-1)/2]$ with weights W_n defined as

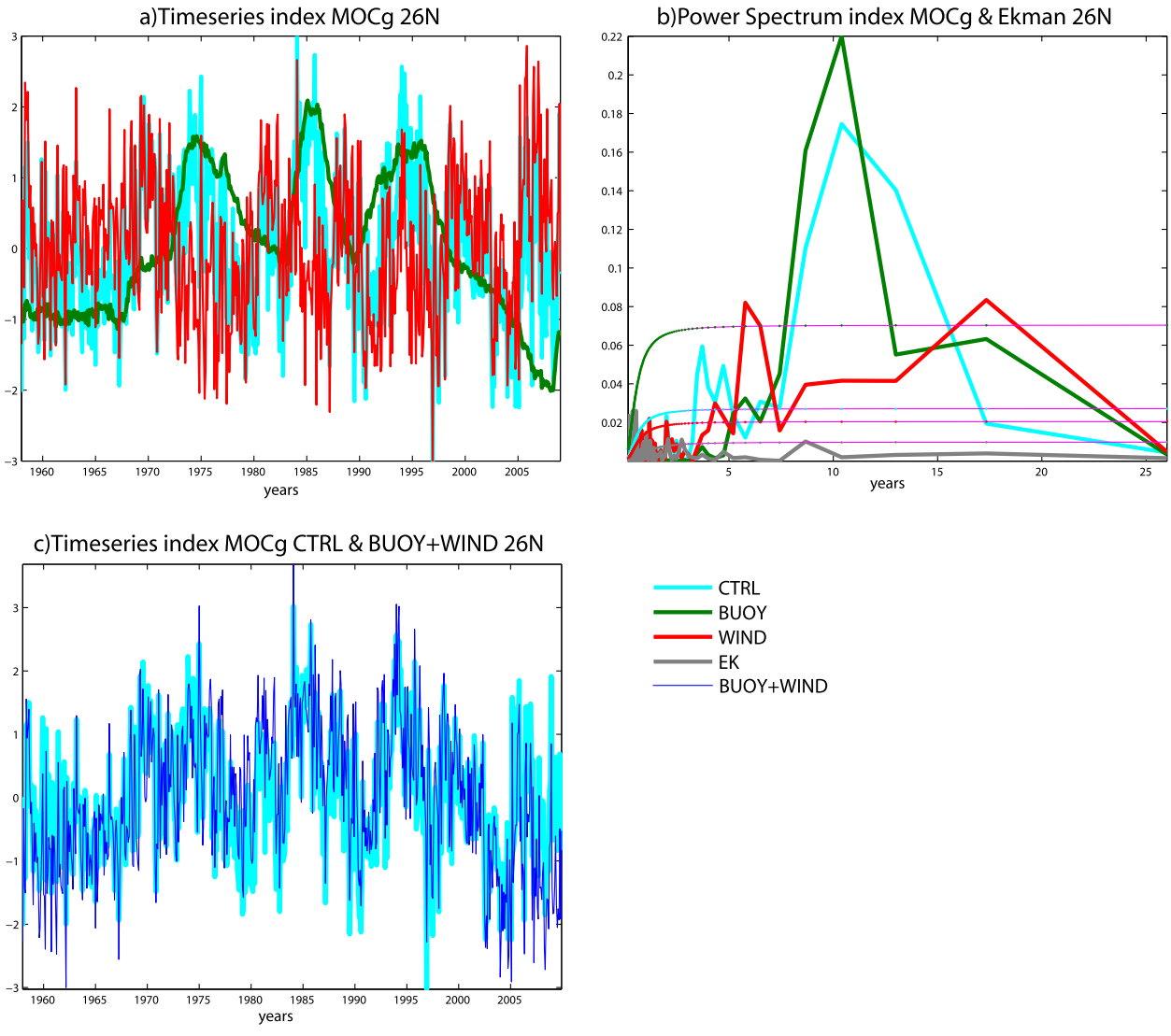

FIG. 1. Variability of the AMOC in the three experiments. (a) Time series of the AMOC index defined as the streamfunction from the total meridional velocity minus the Ekman component and taken at 1162-m depth and 26°N for the three experiments: CTRL experiment (blue line), BUOY experiment (green line), and WIND experiment (red line). The time series have been detrended and the seasonal cycle removed. Finally, the anomalies are standardized. (b) Power spectrum of the time series in (a) obtained using the multitaper method [which provides more degrees of freedom and therefore more significance (Thomson 1982)]. It is tested against the hypothesis that the signal is generated by a first-order autoregressive process [AR(1), yielding a red noise spectrum] and the 95% confidence limit for the rejection of the red noise hypothesis is displayed in magenta lines (note the confidence limit is different for each experiment, denoted by the dots). The gray line is the power spectrum of the Ekman component of the AMOC at 26°N. (c) Time series of the AMOC for the CTRL experiment and the sum of BUOY and WIND experiments.

$$W_n = \begin{cases} 1 - 6\left(\dfrac{|n|}{N/2}\right)^2 + 6\left(\dfrac{|n|}{N/2}\right)^3 & 0 \le |n| \le (N-1)/4 \\ 2\left(1 - \dfrac{|n|}{N/2}\right)^3 & (N-1)/4 \le |n| \le (N-1)/2, \\ 0 & |n| > (N-1)/2 \end{cases} \tag{6}$$

where N is the length of the filter (and the number of months in the cutoff frequency). The frequency bands were chosen to capture the peaks of geostrophic AMOC in the power spectrum (Fig. 1b) and are defined as follows:

intraseasonal to interannual $\psi_{0-3} = \psi' - \psi_{3\text{yr}}$;
interannual to decadal $\psi_{3-7} = \psi_{3\text{yr}} - \psi_{7\text{yr}}$; and
decadal $\psi_{7-13} = \psi_{7\text{yr}} - \psi_{13\text{yr}}$,

where the subscript denotes the length of the filter used, N (i.e., 3 yr = 3*12–1 months). We have tested different filters (i.e., running mean and Lanzcos filter) and the results of the regression analysis do not change substantially. Empirical orthogonal function (EOF) analysis (Bretherton et al. 1992) has also been performed in order to identify the dominant modes of density variability. Maps of different variables regressed onto either the AMOC index or onto principal components (PC) time series from the EOF modes have been statistically tested at the 90% confidence level based on a Student's t test, with effective degrees of freedom reduced following Metz (1991).

3. Results

a. Time scales of the geostrophic component of the AMOC and their related forcing

Figure 1a shows the time series of the monthly anomalies of the geostrophic AMOC index at 26°N for each experiment. Figure 1 suggests that the buoyancy forcing is responsible for the decadal low-frequency variability of the geostrophic transport at 26°N, while the wind forcing is responsible for the interannual and high-frequency variability. This is better illustrated in Fig. 1b, which shows the Fourier spectrum of the AMOC at 26°N in the different simulations.

The AMOC index from the control experiment (CTRL, blue line) shows enhanced spectral density at frequencies of ~9–13 and ~3–5 yr. Both peaks are greater than the 95% confidence level of the first-order autoregressive process [AR(1)], indicating that processes other than just the integration of synoptic weather noise (Hasselmann 1976) are forcing these AMOC oscillations. The decadal peak in the spectrum of the control experiment prominently comes from the buoyancy forcing (BUOY, green line), while the interannual and higher frequencies are dominated by wind forcing (WIND, red line).

The power spectrum of the Ekman AMOC component is also shown in gray in Fig. 1b. The variance of the Ekman component is largely confined to subseasonal and interannual time periods (<2 yr), showing that the variance of the geostrophic AMOC at 26°N is substantially larger than the Ekman component in all three simulations [the geostrophic AMOC explains more than 80% of the total AMOC variance (not shown)].

Finally, we assess the linearity of the decomposition of the AMOC into that which is associated with WIND and BUOY forcing. Figure 1c shows that the majority of the features in the geostrophic AMOC time series at 26°N for the CTRL are reproduced by the sum of the time series of the BUOY + WIND experiments. The correlation coefficient r between the two time series is greater than 0.9, suggesting that, although not perfect, the geostrophic AMOC index is a linear sum of the momentum and buoyancy forcing.

b. Variability of the zonal density gradient at 26°N

In this study we want to understand the processes that relate the density variability to specific forcings and time scales. First, we assess the variability in the zonal density gradient and the modes of density variability on the eastern and western margins.

1) VERTICAL STRUCTURE OF THE ZONAL DENSITY GRADIENT AT 26°N

Figure 2 shows the temporal and vertical structure of the zonal density gradient (eastern boundary minus the western boundary) in all three simulations after removing the seasonal cycle and the linear trend. The boundary density profiles are chosen along the bathymetry at each boundary. It is clear from Fig. 2 that the different forcings have different vertical structure. For the BUOY experiment, the vertical structure of the zonal density gradient shows opposing sign anomalies between 700 and 1500 m and above and below. Below 1500 m, the amplitude of the anomalies in BUOY is substantial down to 4000 m (Fig. 2b). In the WIND experiment there is stronger variability in the upper 1000 m, but the anomalies are small below 2000 m (Fig. 2c). The CTRL experiment shows a pattern that is a mix between both BUOY and WIND experiments (Fig. 2a): specifically, below 2000 m the low-frequency variability follows the BUOY experiment (Fig. 2b), but there a noisier signal in the top 1000 m is similar to the WIND experiment signal (Fig. 2c).

The percentage of the explained variance by each boundary is shown in the right column of Fig. 2. This figure illustrates the explained variance at the different time scales, computed for each integrated depth independently (i.e., $\int_{-h}^{z} (\rho_E - \rho_W)\, dz$). The explained variance is calculated from the square of the correlation coefficient between the anomalous zonal density difference and the anomalous density at each boundary. Note that the percentage does not add up to 100%,

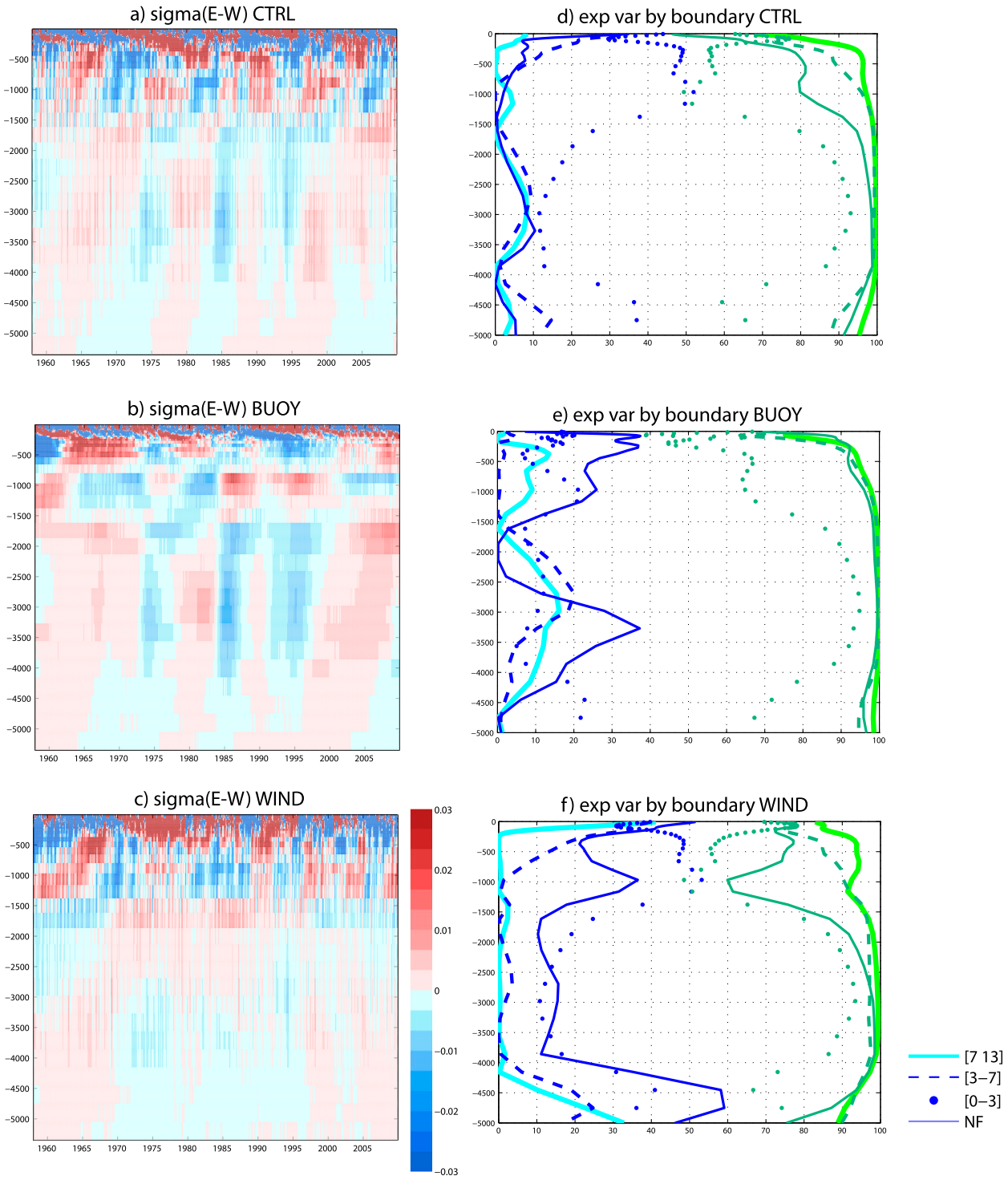

FIG. 2. Character of the zonal density gradient in the three experiments. (left) Depth–time plot of the anomalous zonal density difference at 26°N (σ; kg m^{-3}) at each depth for the three experiments: (a) CTRL experiment, (b) BUOY experiment, and (c) WIND experiment. (right) As in (a)–(c), but for the explained variance of the integrated zonal difference at 26°N by the eastern (blue line) and western (green line) boundary for different time scales after filtering. The explained variance is calculated from the integrated zonal density difference from the bottom to each level of depth.

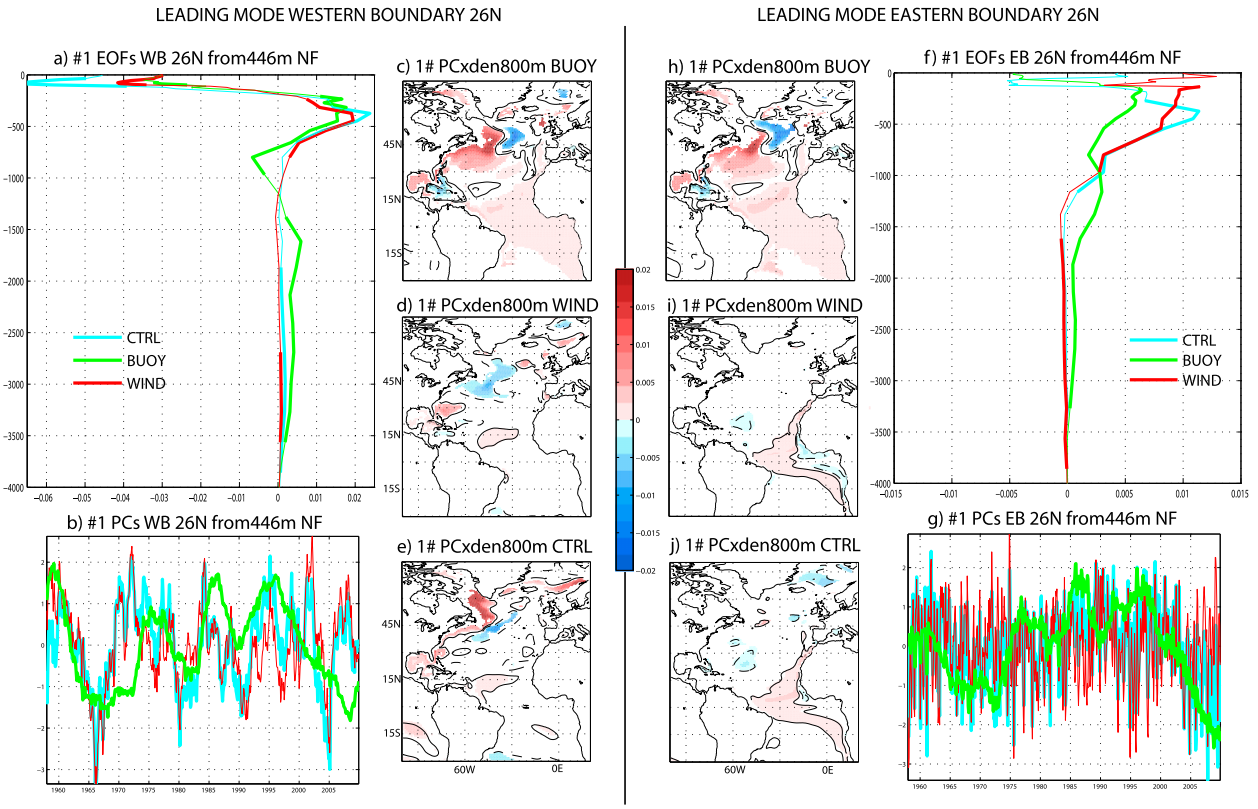

FIG. 3. Leading modes of density variability at 26°N. (left) The (a) leading EOF mode of the anomalous density (σ; kg m^{-3}) of the western boundary at 26°N at each depth for the three experiments: CTRL experiment (blue line), BUOY experiment (green line), and WIND experiment (red line). Thick lines show where the EOF is significant at $\alpha = 0.1$. (b) PCs time series associated with the EOFs in (a). (c) Regression of the density (σ; kg m^{-3}) at 800 m onto the leading variability mode for the BUOY experiment. (d) As in (c), but for the WIND experiment. (e) As in (c) but for the CTRL experiment. (right) (f)–(j) As in (a)–(e), panels but for the eastern boundary.

especially for some depths and frequencies; this is because the boundaries are not independent, as we will see in the following section.

At most frequencies, the western boundary dominates the variance of the zonal density gradient; in particular, the western boundary accounts for over 80% of the variability for all three experiments (see Fig. 2, right column). At higher frequencies, the eastern boundary explains more variance, particularly in the CTRL and WIND experiments. Specifically, the eastern boundary explains up to 50% of the variance in the upper 1500 m at [0–3] yr in both CTRL and WIND (Figs. 2d, 2f), which suggests that the wind drives the variability at the eastern boundary at those time scales in agreement with Chidichimo et al. (2010). Additionally, at [0–3] yr, the eastern boundary also seems to explain part of the zonal gradient in the BUOY experiment at around 1000 m (Fig. 2e).

In summary, the eastern boundary is only important at driving the zonal density gradient at high frequencies (<3 yr), mainly due to wind-forced variability, while the western boundary explains the interannual to decadal variability of the zonal density gradient in both BUOY and WIND experiments.

2) DENSITY VARIABILITY MODES AT 26°N

We now calculate the main modes of density variability for each boundary in order to extract the main processes affecting density. The leading modes of the anomalous density at 26°N for the three simulations are shown in Fig. 3 (representing >60% of the total variance; Table 1) for the western (Figs. 3a–e) and for the eastern boundaries (Figs. 3h–g). The EOF analyses have been performed on the unfiltered time series by considering the density anomalies in the water column below 400 m in order to avoid the highly variable upper ocean. However, the regression of the whole anomalous density profile onto the PCs time series is shown in Fig. 3 to highlight any covariance with the deeper ocean. Additional tests with different depth truncations (the whole column, 400, 800, and 1000 m) have revealed that the modes are sensitive to the chosen truncation level; however, the differences are largely in the percentage of explained variance for each mode (not shown). We have

TABLE 1. Correlation of the PCs' time series and the AMOC index and the percentage of explained variance (in parenthesis) for the first three modes of variability from the unfiltered density variability at 26°N at the western boundary and the eastern boundary and the three simulations. Significant correlations at $\alpha = 0.1$ from a Student's t test are marked with a star. The leading modes are shown in Fig. 3.

	Western boundary			Eastern boundary		
Expt mode	CTRL	BUOY	WIND	CTRL	BUOY	WIND
Leading	0.45* (60)	0.65* (70)	0.21* (61)	−0.05 (68)	0.7* (76)	−0.06 (73)
2	−0.21* (21)	0.72* (14)	−0.22* (27)	0.08 (16)	0.57* (15)	−0.25* (16)
3	0.5* (7)	0.01 (11)	−0.49* (4)	0.23* (10)	0.03 (5)	−0.25* (4)

concluded that the modes of the column below 400 m better represent relevant processes for the AMOC variability, in agreement with the observational work at subannual scales by Chidichimo et al. (2010).

(i) Western boundary

Figure 3a shows the vertical structure of the leading modes of the density anomalies at the western boundary at 26°N for the three experiments. The vertical structure for the three simulations shows a positive (negative) maximum at ~400 m (above 100 m). For the BUOY experiment, negative anomalies are found at 800 m and positive anomalies are present between 1500 and 4000 m. For the CTRL experiment, positive anomalies are also found below 2000 m but with smaller amplitude.

The leading mode reflects low-frequency density variability (Fig. 3b). For the BUOY experiment, the time series are similar to the AMOC index (comparing Fig. 3b with Fig. 1a; $r = 0.65$; Table 1). However, the leading PCs for the WIND and CTRL experiments are very similar ($r = 0.79$) and display an interannual to decadal mode explaining only part of the AMOC (Table 1). The third mode of the CTRL experiment (not shown) is correlated with the leading PC of the BUOY experiment ($r = 0.56$), and it is correlated with the AMOC index ($r = 0.5$; Table 1).

The wider spatial structure of the density anomalies related to the leading EOF modes is shown at the depth of 800 m (Figs. 3c–e). The spatial structure for different levels (500, 1162, 1500 m) is similar (not shown). The BUOY experiment shows a structure with density anomalies over the Labrador and GIN Seas and a spatial pattern that resembles a propagating feature associated with oceanic waves [i.e., anomalies along the boundary in Fig. 3c, similar to Hodson and Sutton (2012)].

For the WIND experiment, the spatial pattern of the leading mode shows positive density anomalies over the Gulf of Mexico, but also anomalous negative densities over mid-Atlantic (Fig. 3d). The leading mode and the third mode (not shown) are found to be part of the same process, but with the third mode lagging the first by ~15 months. This suggests that the mode that is more related with AMOC (number 3, with $r = 0.49$; Table 1) is driven by a wind pattern that has an impact in the mid-Atlantic (Fig. 3d). The wind-related processes will be described later on [section 3c(1)].

(ii) Eastern boundary

Similarly, the leading modes of density variability at 26°N at the eastern boundary are shown in Figs. 3f–j for the three experiments. The vertical structure shows a prominent anomaly in the upper 1000 m for the WIND and the CTRL experiments with significant but small amplitudes below 1500 m (Fig. 3f). For the BUOY experiment there are positive anomalies over most of the water column.

For the BUOY experiment, the leading mode represents the low-frequency variability (Fig. 3g) that is correlated with the AMOC index ($r = 0.7$, Table 1). The leading mode of the eastern boundary in the BUOY experiment depicts the same process as the one described for the leading mode of the western boundary (Fig. 3h compared with Fig. 3c). However, for the WIND and CTRL experiments, the associated time series for the leading mode shows very high-frequency variability (Fig. 3g).

The leading mode for the WIND experiment expresses the subannual density variations (Fig. 3g) that appear to be associated with wind-driven equatorial oceanic waves (Fig. 3i). The second and third modes in the WIND experiment (not shown) present significant correlation with AMOC ($r = 0.25$, Table 1). The three modes describe an instantaneous snapshot in the same propagating wave pattern. This further suggests that density variations at subannual frequencies over the eastern boundary are wind driven and could represent less than 5% of the variability of the AMOC at 26°N.

For the CTRL experiment, the leading mode is similar to the leading mode in the WIND experiment (Fig. 3g; $r = 0.82$). However, the correlation between modes improves if we sum the two time series from the leading modes of both WIND and BUOY experiments (red + green line correlated with the blue line in Fig. 3g; $r = 0.94$). The increase of the correlation suggests that in the CTRL experiment, the subannual frequency variability of density at the eastern boundary, which is wind driven, is modulated by the low-frequency part that is buoyancy forced.

c. *Processes associated with changes in the geostrophic AMOC*

We now try to understand how the anomalous zonal density gradients project onto the AMOC and what processes are at work at different time scales. We will examine the WIND experiment first in section 3c(1), followed by the BUOY experiment in section 3c(2).

1) PROCESSES ASSOCIATED WITH CHANGES IN THE WIND-FORCED AMOC

In this section, we want to understand the geostrophic AMOC response to wind-driven anomalous density patterns. To do so, the unfiltered density anomalies at two specific levels (1160 and 446 m) are projected onto AMOC time series at 26°N for the WIND experiment (Fig. 4). These two levels represent the interior and upper ocean, respectively (note the patterns are not sensitive to the exact depth used). Monthly lags from 2 yr before the AMOC maximum to the simultaneous relationship (i.e., lag 0) are displayed.

Positive density anomalies are present in the mid-Atlantic at ~45°N 2 yr before the AMOC maximum. Coincident positive anomalies are found at 446 m down to ~1160 m (Figs. 4a,b). Moving to shorter lags, the density anomaly appears to propagate westward, reaching the western boundary at lag −15 months (Figs. 4c,d). After reaching the coast, the anomalies appear to travel equatorward along the western boundary reaching the tropics at lag −4 (Figs. 4e,f).

To understand the origin of these density anomalies in the mid-Atlantic and alongshore, we consider the different time scales of the processes involved in the time-evolving density pattern. Figure 5 shows the density anomalies (left) and the Ekman pumping (positive upward) and surface winds (right) regressed on the simultaneous (i.e., lag 0) AMOC variability at high-frequency time-scales of [0–3] yr (note that the pattern is only significant instantaneously). Positive density anomalies, seen along the western boundary (Fig. 5a), are associated with a large-scale wind pattern that resembles a positive NAO-like structure (Fig. 5b). The wind pattern induces anomalous coastal upwelling along the western boundary and, hence, imprints positive density anomalies. This is similar to the wind-forced mechanism found by Köhl (2005) that relates the heaving of isopycnals to local wind-driven coastal up- and downwelling.

Figure 6 shows the filtered anomalies of the density projected onto the AMOC for the [3–7] yr (left), together with the correlation between the AMOC and the surface winds and the related Ekman pumping (right). At lag −24 months, positive density anomalies appear at ~45°N, associated with a cyclonic wind pattern and Ekman upwelling over the mid-Atlantic (Figs. 6a,b). At these frequencies, the atmospheric pattern is significant (in contrast with the unfiltered data, not shown), which suggests that these mechanisms are only important at interannual time scales (i.e., the mechanism is associated with the peak in the spectrum at 5–7 yr in Fig. 1b, red line). From lag −24 to lag −8, the cyclonic wind pattern appears to persist in the regression and the density anomalies appear to propagate westward (Figs. 6a–g).

From Figs. 4–6, we conclude that two processes are important for the wind to generate density anomalies that, in turn, affect the geostrophic AMOC transports at 26°N: (i) locally generated by the wind forcing via coastal upwelling, and (ii) remotely generated by large-scale wind anomalies in the mid-Atlantic via Ekman pumping at the [3–7]-yr frequency band. Because of the leading relationship, the remote wind-forcing mechanism entails some potential predictability, while the local coastal density anomalies occur simultaneously with the wind at very high frequencies and are thus unpredictable.

(i) *Mechanisms at work in the remotely wind-generated density anomalies*

As explained above, the wind-driven interannual variability of the AMOC originates from a large-scale cyclonic wind pattern in the mid-Atlantic (Fig. 6b). This large-scale wind pattern appears to create density anomalies ~45°N that are related to Ekman pumping (Figs. 6a,b). The analysis suggests that these density anomalies present evidence of southwestward propagation reaching the western boundary (Fig. 4), consistent with planetary Rossby waves. However, a simple analysis of the propagation speed [assuming a baroclinic Rossby wave mode calculated following Pedlosky (1979) and Gill (1982)] suggests that Rossby waves would take substantially longer than a year to travel from 45°N, 45°W to 37°N, 60°W. On the other hand, the wind pattern, and hence the Ekman pumping anomalies, also appears to persist in time and propagate westward (Fig. 6). Such a westward propagation of the wind pattern likely highlights that Rossby waves are induced closer to the western boundary at shorter lead times (i.e., because shorter distances can be traversed at shorter leads). A similar mechanism was found to be important in Cabanes et al. (2008).

Although the density anomalies appear to originate at ~45°N at −24 months lead (see Figs. 4a, 6a), the Ekman pumping anomalies do not appear to be collocated with the density anomalies and appear farther south (see Fig. 6b). The discrepancy in position suggests that not all of the density anomalies in the central Atlantic are simply

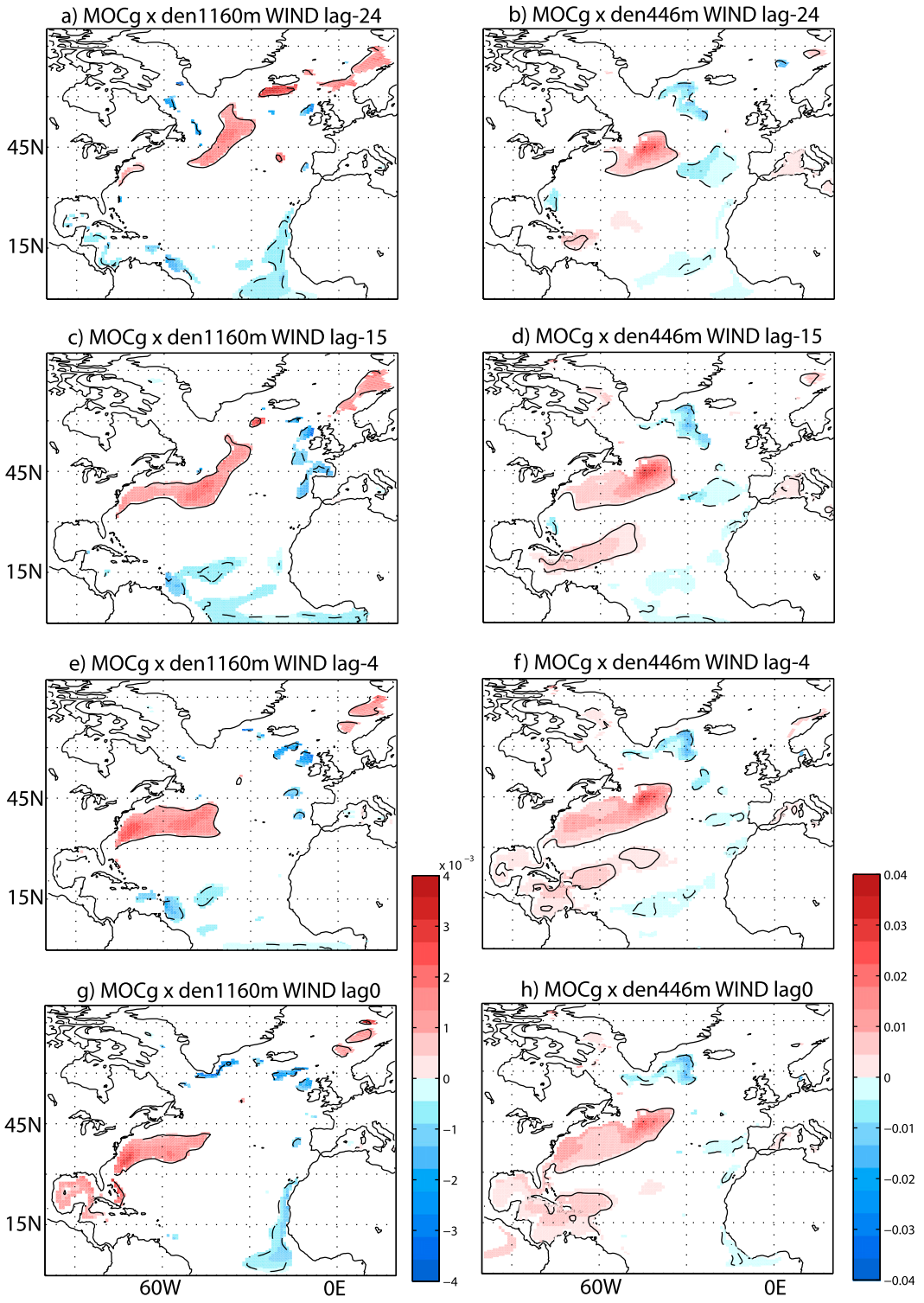

FIG. 4. Density anomalies associated with AMOC changes in the WIND experiment. (a) Anomalous density (σ; kg m^{-3}) at 1162-m depth regressed onto the geostrophic AMOC time series at 26°N for the WIND experiment 24 months in advance. Shaded areas are significant at $\alpha = 0.1$, and the 0.2 correlation isoline is plotted in black. (b) As in (a), but for 446 m. (c),(d) As in (a),(b), but for lag −15 months. (e),(f) As in (a),(b), but for lag −4. (g),(h) As in (a) and (b), but for simultaneous (i.e., 0) lag.

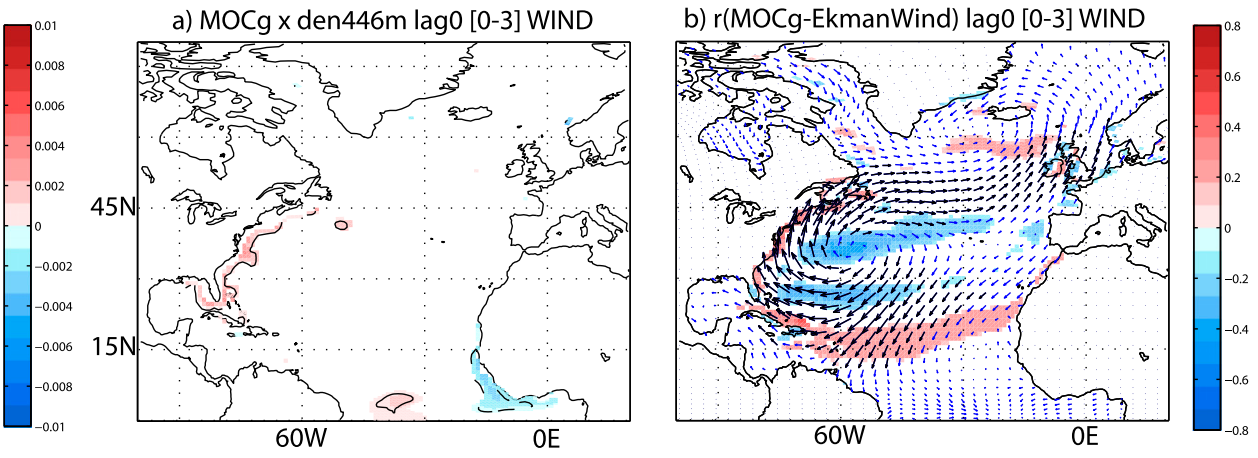

FIG. 5. Anomalies associated with AMOC changes in the WIND experiment at periods <3 yr. (a) Anomalous density (σ; kg m^{-3}) at 446-m depth regressed onto the geostrophic AMOC time series at 26°N filtered in the band of [0–3]-yr periodicity for the WIND experiment at simultaneous lag. Shaded areas are significant at $\alpha = 0.1$ significant level, and the 0.2 correlation isoline is plotted in black. (b) Correlation map between the geostrophic AMOC and the surface wind (vectors are black when it is significant at $\alpha = 0.1$, otherwise they are blue) and Ekman pumping (areas are shaded at $\alpha = 0.1$ significant level) filtered in the band of [0–3]-yr periodicity for the wind forcing simulation at simultaneous lag.

due to Ekman upwelling. Further examination suggested that the density anomalies at ~45°N are a result of circulation changes in the Gulf Stream extension, which could be related to the intergyre gyre (Marshall et al. 2001, not shown). However, the circulation change did not appear to be simply related through Sverdrup balance to wind stress curl over the subtropical gyre, but instead appeared to be also be lagging (by over a year) wind stress anomalies north of 45°N (not shown). Regardless of the exact origin of the density anomalies, the analysis here suggests that the anomalous cyclonic wind structure over the mid-Atlantic is a potential source of interannual variability for the geostrophic transports at 26°N.

(ii) Local versus remote wind-driven density signals

We now evaluate the relative importance of the local wind for driving density anomalies on the western boundary versus the remotely generated mechanism in the mid-Atlantic. To do this we remove the instantaneous (i.e., lag zero) coastal upwelling signal by regressing the density anomalies onto the alongshore wind between 20° and 40°N on the western boundary (see green box on Fig. 7a). To ensure that we remove the local wind forcing that is represented in Fig. 5, we have filtered the density anomalies and the wind variations at the [0–3]-yr periodicity band. The pattern of density anomalies is shown in Fig. 7a and is very similar to the one shown in Fig. 5a. The coastal upwelling signal on the western boundary is then removed from the nonfiltered density anomalies at all months by using the pattern in Fig. 7a scaled by the wind stress index. The remaining density anomalies are then projected back onto AMOC (see Fig. 7b). The resulting pattern shown in Fig. 7b is similar to the projection of the nonfiltered density anomalies onto the AMOC (Fig. 4h). The ratio between the projection of the density minus the signal due to the local wind onto the AMOC at 26°N (Fig. 7b) and the projection of the total (unfiltered) density signal onto the AMOC at 26°N (Fig. 4h) is displayed in Fig. 7c (colors are only shown where both signals are significant). Figure 7c reveals that the remote forcing explains more than 70% of the density variability along the western boundary that is associated with the AMOC when compared with the local wind. A similar percentage is also found at 1160-m depth (not shown). We also tested the sensitivity to the use of temporal filtering to calculate the effect of the local wind on density (i.e., on Fig. 7a). Although there are some differences in the details of the regression of density onto the wind index (particularly on the significance of the pattern; not shown), we found that the ratio (i.e., Fig. 7c) is not sensitive to the use of filtered anomalies as opposed to unfiltered (not shown). Therefore, Fig. 7c strongly suggests that the geostrophic AMOC variance that is related directly to the momentum forcing is dominated by remotely generated density anomalies.

2) PROCESSES ASSOCIATED WITH CHANGES IN THE BUOYANCY-FORCED AMOC

In this section, the processes associated with the buoyancy-driven AMOC are investigated. Figure 8 (left column) shows the unfiltered density anomalies at 1160 m regressed onto AMOC at 26°N for different lags, where the signal is clearest. Preexisting anomalies are

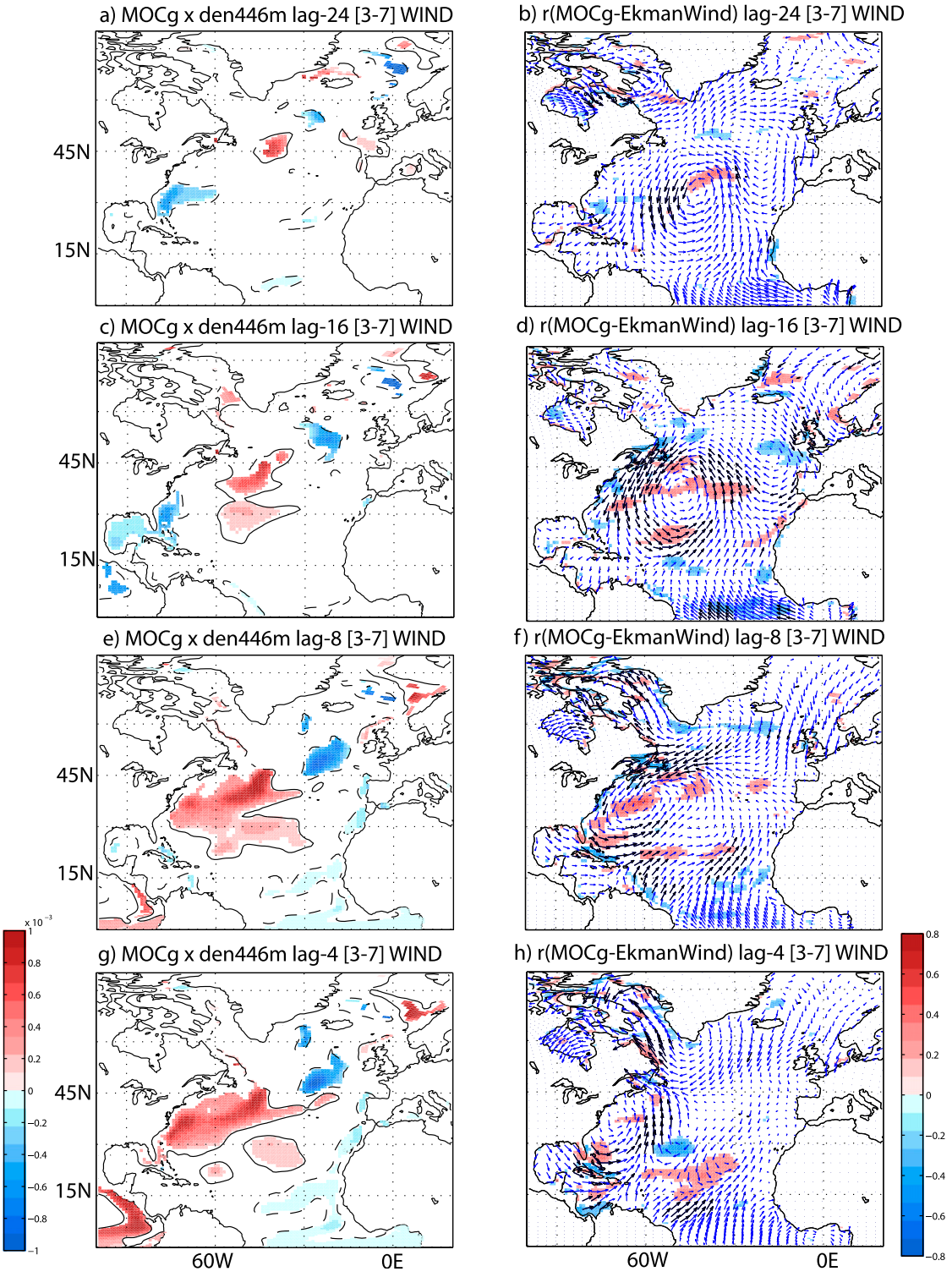

FIG. 6. Anomalies associated with AMOC changes in the WIND experiment at periods [3–7] yr. (a) Anomalous density (σ; kg m^{-3}) at 446-m depth regressed onto the geostrophic AMOC time series at 26°N filtered in the band of [3–7]-yr periodicity for the WIND experiment 24 months in advance. Shaded areas are significant at $\alpha = 0.1$, and the 0.2 correlation isoline is plotted in black. (b) Correlation map between the geostrophic AMOC and the surface wind (vectors are black when it is significant at $\alpha = 0.1$, otherwise they are blue) and Ekman pumping (areas are shaded at the $\alpha = 0.1$ significant level) filtered in the band of [3–7]-yr periodicity for the WIND experiment 24 months in advance. (c),(d) As in (a),(b), but for the lag −16 months. (e),(f) As in (a),(b), but for the lag −8 months. (g),(h) As in (a),(b), but for the lag −4 months.

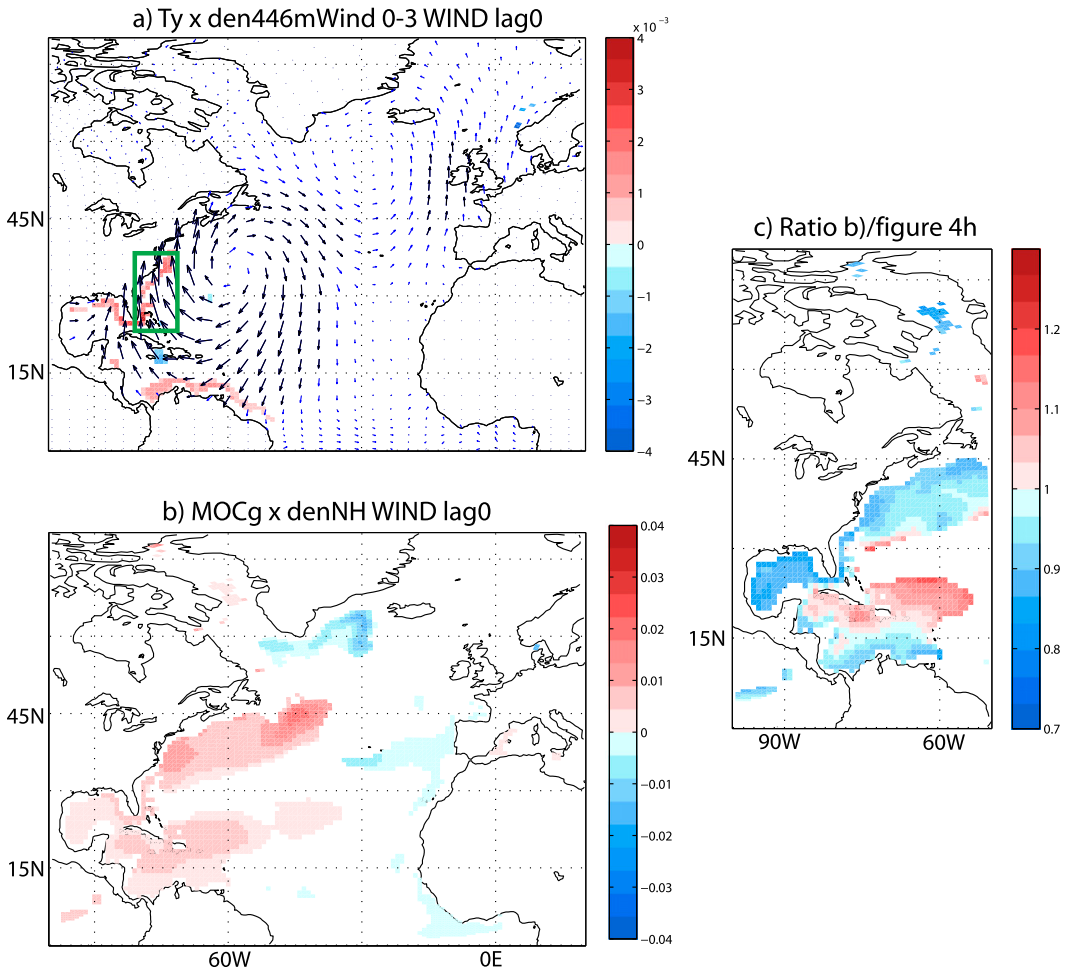

FIG. 7. Exploring the importance of local coastal Ekman upwelling and remote Ekman upwelling in driving density anomalies in the WIND simulation. (a) Regression of the anomalous density at 446-m depth and surface winds onto a local wind index (defined as the meridional surface wind averaged over 20°–40°N, 80°–70°W, green box) filtered in the band of [0–3]-yr periodicity for the WIND experiment and simultaneous lag. Only significant anomalies at $\alpha = 0.1$ have been shaded. This represents the impact of coastally induced Ekman upwelling at the western boundary on the density field. (b) Regression of the anomalous density at 446 m after the signal of the local wind has been removed onto the unfiltered geostrophic AMOC at 26°N for the WIND experiment at simultaneous lag. (c) Illustration of (b) divided by the unfiltered density anomalies regressed onto the AMOC (Fig. 4h), which shows the relative importance of the local (simultaneous) and remote impact of the wind. Note the ratio is only shown where signal in Figs. 7b and 4h are significant at $\alpha = 0.1$.

found over the western and central part of the basin that likely relates to previous adjustments of the AMOC. However, ~3–4 yr before a peak of the AMOC, positive density anomalies appear in the Labrador Sea (Fig. 8a). The density anomalies propagate southward as it has been theorized by Johnson and Marshall (2002) and shown in other GCM studies (Zhang 2010; Hodson and Sutton 2012).

The regression of the SLP (filtered at the 7–13-yr frequency band) onto the AMOC for different lags (Fig. 8, right column) reveals that low-frequency NAO-like forcing is behind the changes in water properties in the Labrador and GIN Seas in this model. The importance of the NAO is in agreement with previous modeling studies (Delworth and Greatbatch 2000; Eden and Willebrand 2001; Ortega et al. 2011; Robson et al. 2012). Correlation analysis between the NAO (calculated as the difference in SLP between the two pressure systems; the subtropical high at 40°–45°N, 30°–15°W and the subpolar low at 65°–70°N, 30°–15°W) and the AMOC index exhibits significant positive correlation ($r > 0.6$) when the NAO is leading the AMOC by 2–4 yr (not shown).

The driving of the AMOC by the buoyancy forcing related to the NAO is consistent with other works (Delworth and Greatbatch 2000; Eden and Willebrand

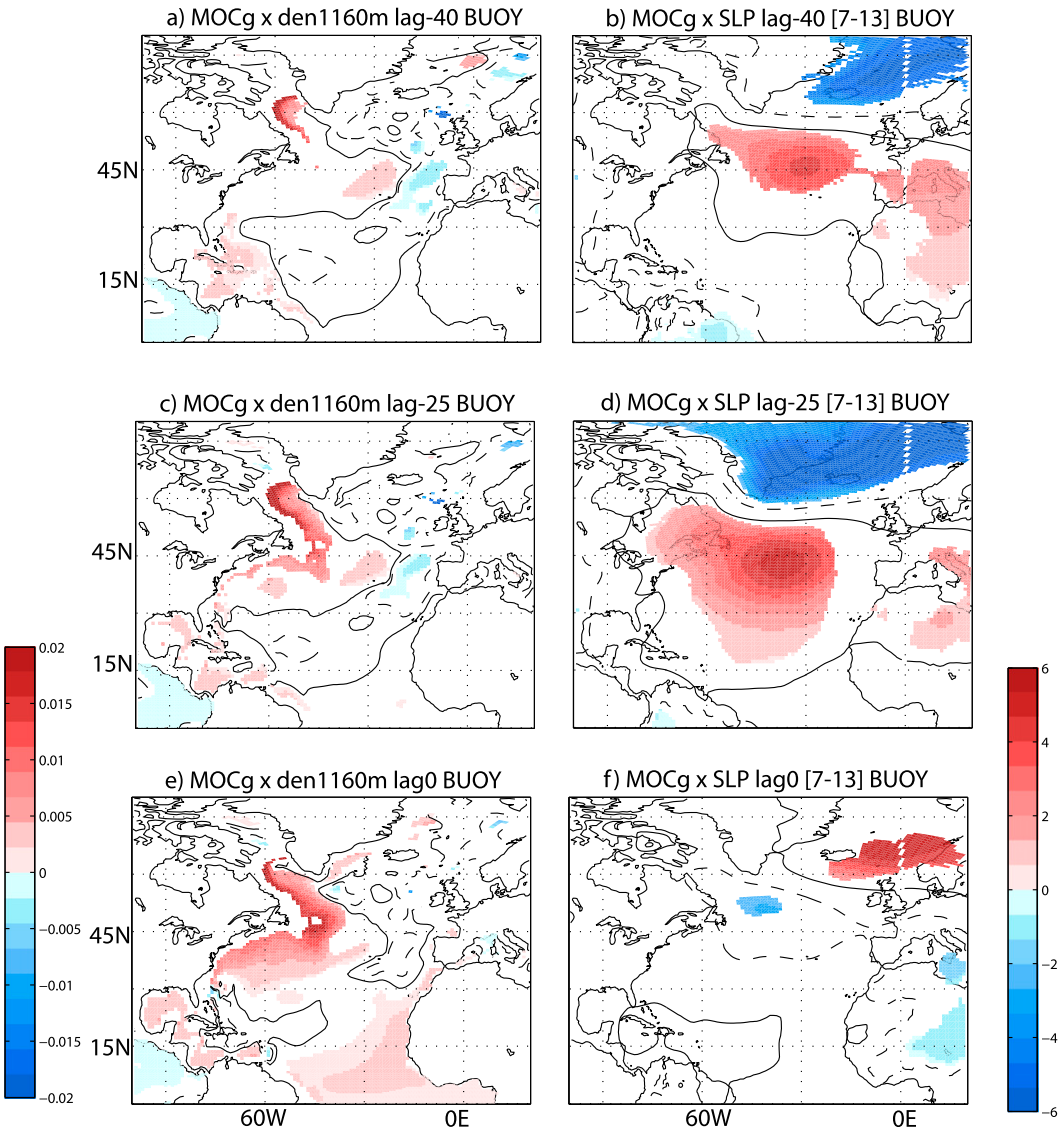

FIG. 8. Density anomalies associated with changes in AMOC in the BUOY experiment. (a) Anomalous density (σ; kg m^{-3}) at 1162-m depth regressed onto the geostrophic unfiltered AMOC time series at 26°N for the BUOY experiment 40 months in advance. Shaded areas are significant at $\alpha = 0.1$, and the 0.2 correlation isoline is plotted in black. (b) Anomalous SLP (in hPa) regressed onto the geostrophic AMOC at 26°N filtered in the band of [7–13]-yr periodicity for the BUOY experiment 40 months in advance. (c),(d) as in (a),(b), but for lag −25 months. (e),(f) as in (a),(b), but for simultaneous lag.

2001; Persechino et al. 2012; Robson et al. 2012; Yeager and Danabasoglu 2014; among others). A positive (negative) NAO pattern increases (decreases) the surface heat loss, which, in turn, increases (decreases) the density over the Labrador Sea (Figs. 8a,b) and enhances (weakens) the deep convection (Biastoch et al. 2008). The oceanic adjustment occurs through planetary waves or advection; coastally trapped density anomalies propagate southward and then eastward across the equator.

4. Discussion

Processes in the control experiment

To understand whether the different mechanisms seen in both the BUOY and WIND experiments are at work in the CTRL experiment, regression maps have been computed for the CTRL experiment. Figure 9 shows the density anomalies regressed onto the AMOC from the CTRL experiment and for different lags (the same as Fig. 4 but now for CTRL). Two years before,

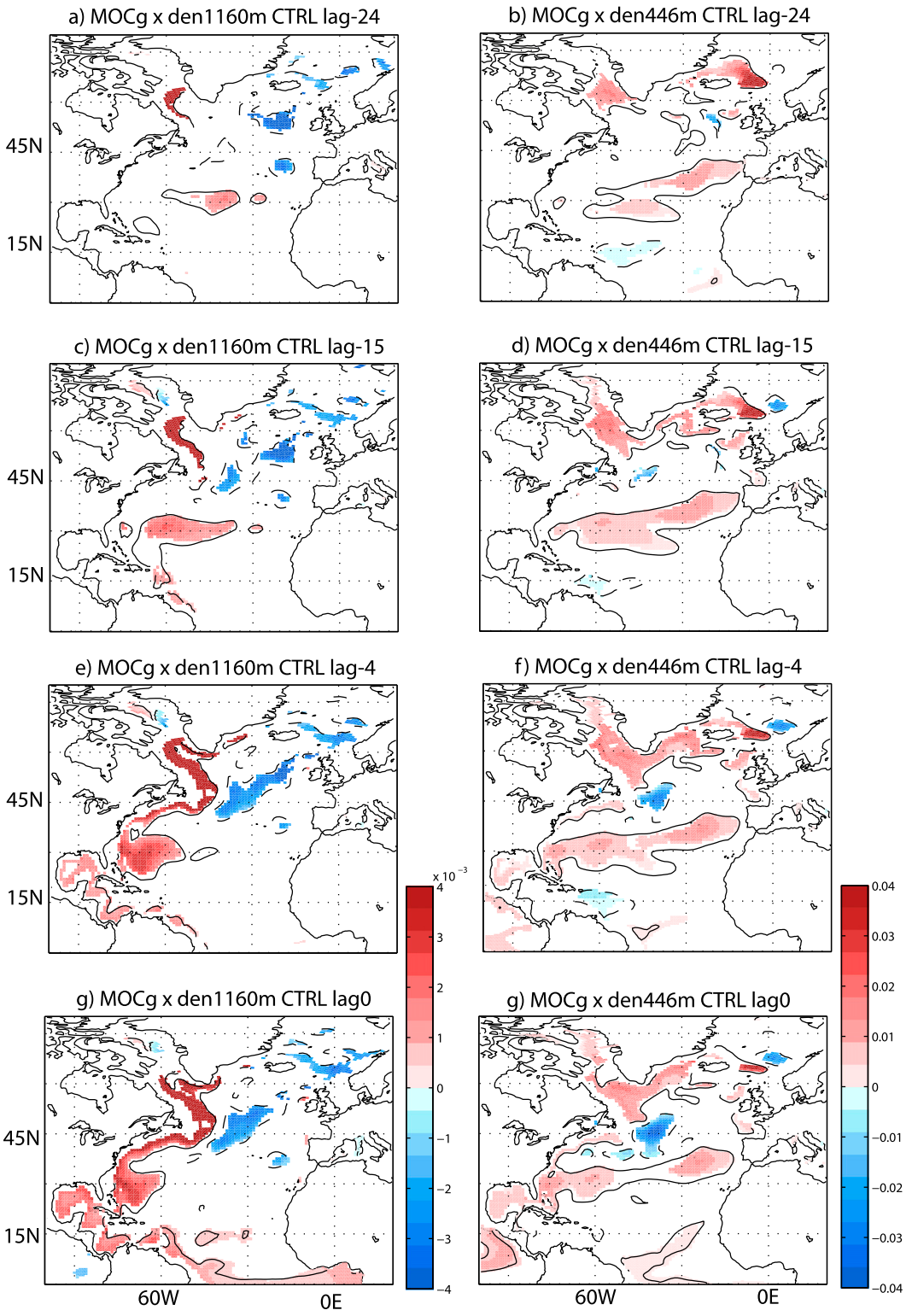

FIG. 9. Density anomalies associated with changes in the AMOC in the CTRL experiment. (a) Anomalous density (σ; kg m^{-3}) at 1162-m depth regressed onto the geostrophic AMOC time series at 26°N for the CTRL experiment 24 months in advance. Shaded areas are significant at $\alpha = 0.1$, and the 0.2 correlation isoline is plotted in black. (b) As in (a), but for the level 446 m. (c),(d) As in (a),(b), but for lag −15 months. (e),(f) As in (a),(b), but for lag −4. (g),(h) As in (a),(b), but for simultaneous lag.

AMOC maximum positive density anomalies occur in the mid-Atlantic around 30°N (Figs. 9a,b). The density anomalies over the mid-Atlantic appear to propagate westward (Fig. 9). In addition, positive density anomalies occur over the Labrador and GIN Seas (Figs. 9a,b). The density anomalies from the Labrador Sea propagate equatorward along the western boundary, and at lag −4, the density anomalies are no longer distinct from those propagating from the interior.

To understand the processes at work, and the frequency dependence of the anomalies, we have plotted the regression maps for specific frequency bands (Fig. 10). At interannual time scales ([3–7]-yr frequency band), density anomalies appear at ~45°N 2 yr before a maximum of the AMOC. However, the wind structure is different to that seen in the WIND experiment at this lead (Fig. 6b); in particular, strong westerly winds appear north of 55°N (60°N, 50°W, Fig. 10b). Around 15 months before a maximum of the AMOC, a cyclonic wind pattern and the associated Ekman pumping are visible in the mid-Atlantic (Fig. 10d), which produces density anomalies across the basin (north of 30°N from 60° to 30°W, Fig. 10c) that propagate westward (Figs. 10c,e). This pattern is similar to that described for the WIND experiment in Fig. 6b. At interannual to decadal time scales in the CTRL experiment ([3–7]-yr time scale; Fig. 10), density anomalies over the Labrador Sea are also present, but their southward propagation is less clear. At decadal time scales (not shown), the density pattern is similar to the density signal in Fig. 8a from the BUOY experiment. Finally, the high-frequency timescale (<3 yr) local wind stress at 26°N, which is related to a positive NAO-like pattern, drives Ekman-induced coastal upwelling that amplifies the density anomalies along the western boundary (Figs. 10g,h).

Although the mechanisms extracted from BUOY and WIND experiments are found to be present in the CTRL experiment, there are differences. In particular, at interannual time scales, the majority of wind-driven density anomalies in the North Atlantic interior appear farther south in the CTRL experiment than in the WIND experiment (cf. Fig. 6c and Fig. 10c). The peak in the power spectrum at interannual to decadal time scales also appears at different time scales between the CTRL and WIND simulation; the CTRL experiment yields an oscillation period of about 3–5 yr, while the WIND experiment indicates a time scale of about 5–7 yr (Fig. 1b). We have noticed that there are some differences between the experiments, which could impact the time scale of the mechanisms. In particular, a northward shift in the mean Gulf Stream position in the WIND experiment relative to the CTRL, and its resultant impact on the stratification, could account for some of the difference by slowing the westward propagation speed of the features (Gill 1982). However, despite these differences in time scales, the similarity between density patterns for CTRL and WIND experiments at interannual to decadal time scales suggests that wind stress curl in the central Atlantic significantly impacts the strength of the AMOC on multiannual time scales.

5. Conclusions

The processes influencing the density variations at the boundaries of the Atlantic at 26°N have been evaluated with a set of OGCM simulations. The main mechanisms for the WIND and BUOY experiment are described in Fig. 11. The percentage of the explained AMOC variance by each mechanism has been estimated from the square correlation coefficient between the PC representing each process and the AMOC index, weighted by how much density variance the EOF is actually explaining (i.e., fraction of variance = $r^2 \times$ eigenvalue). The main findings can be summarized as follows:

- Both wind stress and variations in the surface buoyancy fluxes contribute to the variability of the geostrophic part of the AMOC at 26°N. In the numerical experiments used here, fluctuations related to the wind stress are mostly confined to intraseasonal and interannual time scales, whereas the buoyancy forcing leads to variations on interannual to decadal time scales (Fig. 1).
- Low-frequency variability of the zonal density gradients is dominated by changes on the western boundary for the three experiments; more than 90% of the variance is explained by the western boundary below 200 m at both decadal time scales and interannual time scales (>3 yr) (Fig. 2).
- The eastern margin accounts for high-frequency variability (<3 yr) that is mainly wind driven. Density anomalies in the eastern boundary can explain up to ~50% of the variability of the zonal density gradients in the water column within 100–1500-m depth on those time scales (Fig. 2).
- The vertical structure of the leading density variability mode at 26°N at the western boundary shows a prominent peak at 446 m for the three simulations. The leading mode for the WIND experiment projects onto the density anomalies from 100 m down to 1000 m, with a significant signal in depth (3000–3500 m). However, only BUOY and CTRL experiments have a coherent and significant signal below 1000–3500 m (Fig. 3).
- In the BUOY experiment, the leading modes of density variations in the water column at 26°N for both margins are explained by the same basin-scale

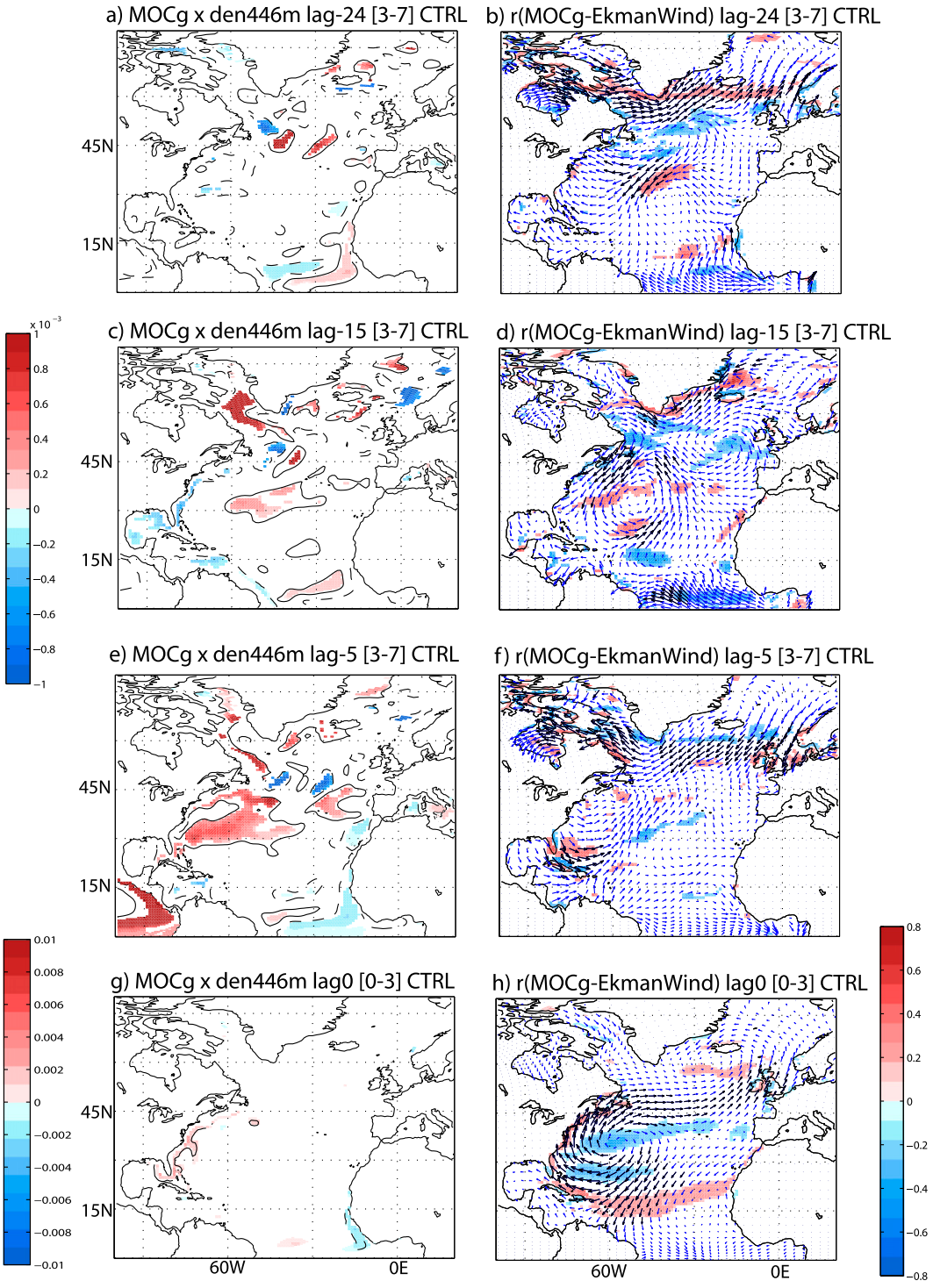

FIG. 10. Anomalies associated with AMOC changes in the CTRL experiment at different periodicities. (a) Anomalous density (σ; kg m^{-3}) at 446-m depth regressed onto the geostrophic AMOC time series at 26°N filtered in the band of [3–7]-yr periodicity for the CTRL experiment 24 months in advance. Shaded areas are significant at $\alpha = 0.1$, and the 0.2 correlation isoline is plotted in black. (b) Correlation map between the geostrophic AMOC and the surface wind (vectors are black when it is significant at $\alpha = 0.1$, otherwise they are blue) and Ekman pumping (areas are shaded at $\alpha = 0.1$ significant level) filtered in the band of [3–7]-yr periodicity for the CTRL experiment 24 months in advance. (c),(d) As in (a),(b), but for the lag −15 months. (e),(f) As in (a),(b), but for the lag −5 months. (g),(h) As in (a),(b), but for the band of [0–3]-yr periodicity and for the simultaneous lag.

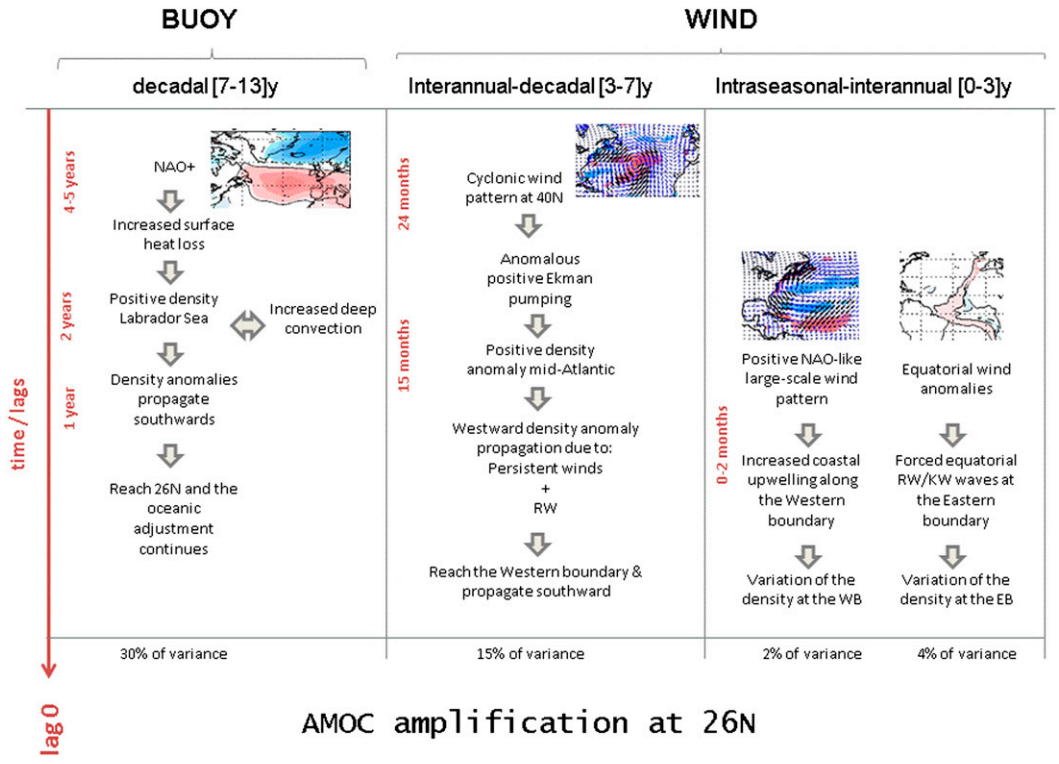

FIG. 11. Summary of the processes described for the BUOY and WIND experiments. Percentage of AMOC variance at 26°N is computed from the square correlation coefficients between the geostrophic AMOC time series and the PC that represents such process (r^2 in Table 1) considering how much density variance the EOF explains (i.e., $[\lambda_k/\sum_{k=1}^{K}\lambda_k]$*100, where λ is the corresponding eigenvalue of the kth mode).

process, which is related to the creation of density anomalies over the Labrador Sea at decadal time scales.

- In the WIND experiment, both margins appear independent and describe different processes: the leading mode for the western boundary is related to the large-scale wind structure in the mid-Atlantic, while the leading mode for the eastern boundary primarily represents subannual variability related to equatorial waves (Fig. 3).
- Wind can induce local density anomalies that affect the AMOC instantaneously via coastal upwelling/downwelling, but also via Ekman pumping variations in the mid-Atlantic. The remote wind anomalies appear to explain more than 70% of the WIND-forced AMOC-related density variance at 26°N.
- Up to 2 yr before, the maximum of the AMOC large-scale wind anomalies can create density anomalies through Ekman pumping, which then propagate westward and interact with the western boundary (Figs. 4, 6). This remote forcing mechanism occurs from interannual to decadal time scales and accounts for ~15% of the interannual total variance in the WIND experiment.
- Buoyancy-driven decadal AMOC variability is related to the NAO, which leads to changes in deep-water formation over the Labrador Sea, consistent with previous studies (i.e., Delworth and Greatbatch 2000). Anomalous densities propagate equatorward along the western boundary and throughout the equatorial waveguide, completing the ocean adjustment (Fig. 8).

We have shown further convincing results that wind forcing is important for multiannual variability of the AMOC, which could give some potential predictability of the AMOC. Nevertheless, we note that there are several limitations in the methodology used here. For instance, (i) we have analyzed only one model, that is, different models resolve key processes in the ocean response differently, such as deep-water formation regions (Mignot and Frankignoul 2005) and the Gulf Stream path and strength (de Coëtlogon 2006). (ii) Our model could be too coarse resolution for a proper simulation of coastal waves (Getzlaff et al. 2005; Hodson and Sutton 2012). (iii) The three experiments analyzed here consist of only 50 yr of integrations that could be too short in order to assert conclusions on decadal to multidecadal variability. A multimodel study with longer simulations

would be useful for a better assessment of the proposed mechanisms. Finally, analysis of an ensemble of runs would give more insights of the importance of the different mechanisms when both wind and buoyancy forcing are operating. Further work will be necessary in order to understand the relative importance of the remote wind-driven mechanism in the real world. To do so, analysis of the ocean reanalysis as well as the observational RAPID array could be investigated. The separation between the wind (momentum) and buoyancy forcings and how they act at different time scales could be useful for future interpretation of the observational record.

Acknowledgments. IP and JR were supported by the NERC funded VALOR project (NE/G007845/1) and by the BNP Paribas foundation via the PRECLIDE project under the CNRS Research Convention Agreement 30023488. We thank the anonymous reviewers for their useful comments.

REFERENCES

Adcroft, A., C. Hill, and J. Marshall, 1997: Representation of topography by shaved cells in a height coordinate ocean model. *Mon. Wea. Rev.,* **125,** 2293–2315, doi:10.1175/1520-0493(1997)125<2293:ROTBSC>2.0.CO;2.

Baehr, J., J. Hirschi, J. O. Beismann, and J. Marotzke, 2004: Monitoring the meridional overturning circulation in the North Atlantic: A model-based array design study. *J. Mar. Res.,* **62,** 283–312, doi:10.1357/0022240041446191.

Balan Sarojini, B., and Coauthors, 2011: High frequency variability of the Atlantic meridional overturning circulation. *Ocean Sci. Discuss.,* **8,** 219–246, doi:10.5194/osd-8-219-2011.

Balmaseda, M. A., and K. Mogensen, 2010: Evaluation of ERA-Interim forcing fluxes from an ocean perspective. Issue 6 of ERA Rep. Series, 9 pp.

——, ——, and A. T. Weaver, 2013: Evaluation of the ECMWF Ocean Reanalysis System ORAS4. *Quart. J. Roy. Meteor. Soc.,* **139,** 1132–1161, doi:10.1002/qj.2063.

Barnier, B., and Coauthors, 2006: Impact of partial steps and momentum advection schemes in a global ocean circulation model at eddy-permitting resolution. *Ocean Dyn.,* **56,** 543–567, doi:10.1007/s10236-006-0082-1.

Bentsen, M., H. Drange, T. Furevik, and T. Zhou, 2004: Simulated variability of the Atlantic meridional overturning circulation. *Climate Dyn.,* **22,** 701–720, doi:10.1007/s00382-004-0397-x.

Biastoch, A., C. W. Boning, J. Getzlaff, J. M. Molines, and G. Madec, 2008: Causes of interannual–decadal variability in the meridional overturning circulation of the midlatitude North Atlantic Ocean. *J. Climate,* **21,** 6599–6615, doi:10.1175/2008JCLI2404.1.

Blanke, B., and P. Delecluse, 1993: Variability of the tropical Atlantic Ocean simulated by a general circulation model with two different mixed-layer physics. *J. Phys. Oceanogr.,* **23,** 1363–1388, doi:10.1175/1520-0485(1993)023<1363:VOTTAO>2.0.CO;2.

Böning, C. W., M. Scheinert, J. Dengg, A. Biastoch, and A. Funk, 2006: Decadal variability of subpolar gyre transport and its reverberation in the North Atlantic overturning. *Geophys. Res. Lett.,* **33,** L21S01, doi:10.1029/2006GL026906.

Bretherton, S. B., C. Smith, and J. H. Wallace, 1992: An intercomparison of methods for finding coupled patterns in climate data. *J. Climate,* **5,** 541–560, doi:10.1175/1520-0442(1992)005<0541:AIOMFF>2.0.CO;2.

Cabanes, C., T. Lee, and L.-L. Fu, 2008: Mechanisms of interannual variations of the meridional overturning circulation of the North Atlantic Ocean. *J. Phys. Oceanogr.,* **38,** 467–480, doi:10.1175/2007JPO3726.1.

Chidichimo, M. P., T. Kanzow, S. A. Cunningham, W. E. Johns, and J. Marotzke, 2010: The contribution of eastern-boundary density variations to the Atlantic meridional overturning circulation at 26.5°N. *Ocean Sci.,* **6,** 475–490, doi:10.5194/os-6-475-2010.

Cunningham, S. A., and R. Marsh, 2010: Observing and modelling changes in the Atlantic MOC. *Wiley Interdiscip. Rev.: Climate Change,* **1,** 180–191, doi:10.1002/wcc.22.

——, and Coauthors, 2007: Temporal variability of the Atlantic meridional overturning circulation at 26.5°N. *Science,* **317,** 935–938, doi:10.1126/science.1141304.

de Coëtlogon, G., C. Frankignoul, M. Bentsen, C. Delon, H. Haak, S. Masina, and A. Pardaens, 2006: Gulf stream variability in five oceanic general circulation models. *J. Phys. Oceanogr.,* **36,** 2119–2135, doi:10.1175/JPO2963.1.

Dee, D. P., and Coauthors, 2011: The ERA-Interim reanalysis: Configuration and performance of the data assimilation system. *Quart. J. Roy. Meteor. Soc.,* **137,** 553–597, doi:10.1002/qj.828.

Delworth, T. L., and R. J. Greatbatch, 2000: Multidecadal thermohaline circulation variability driven by atmospheric surface flux forcing. *J. Climate,* **13,** 1481–1495, doi:10.1175/1520-0442(2000)013<1481:MTCVDB>2.0.CO;2.

Dong, B., and R. Sutton, 2001: The dominant mechanism of variability in Atlantic Ocean heat transport in a coupled ocean-atmosphere GCM. *Geophys. Res. Lett.,* **28,** 2445–2448, doi:10.1029/2000GL012531.

——, and ——, 2005: Mechanism of interdecadal thermohaline circulation variability in a coupled ocean–atmosphere GCM. *J. Climate,* **18,** 1117–1135, doi:10.1175/JCLI3328.1.

Eden, C., and T. Jung, 2001: North Atlantic interdecadal variability: Oceanic response to the North Atlantic Oscillation (1865–1997). *J. Climate,* **14,** 676–691, doi:10.1175/1520-0442(2001)014<0676:NAIVOR>2.0.CO;2.

——, and J. Willebrand, 2001: Mechanism of interannual to decadal variability of the North Atlantic circulation. *J. Climate,* **14,** 2266–2280, doi:10.1175/1520-0442(2001)014<2266:MOITDV>2.0.CO;2.

Frankignoul, C., G. de Coëtlogon, T. M. Joyce, and S. Dong, 2001: Gulf Stream variability and ocean–atmosphere interactions. *J. Phys. Oceanogr.,* **31,** 3516–3529, doi:10.1175/1520-0485(2002)031<3516:GSVAOA>2.0.CO;2.

Gent, P. R., and J. C. McWilliams, 1990: Isopycnal mixing in ocean circulation models. *J. Phys. Oceanogr.,* **20,** 150–155, doi:10.1175/1520-0485(1990)020<0150:IMIOCM>2.0.CO;2.

Getzlaff, J., C. W. Böning, C. Eden, and A. Biastoch, 2005: Signal propagation in the North Atlantic overturning. *Geophys. Res. Lett.,* **32,** L09602, doi:10.1029/2004GL021002.

Gill, A. E., 1982: *Atmosphere–Ocean Dynamics.* Academic Press, 662 pp.

Grötzner, A., M. Latif, and T. P. Barnett, 1998: A decadal climate cycle in the North Atlantic Ocean as simulated by the ECHO coupled GCM. *J. Climate,* **11,** 831–847, doi:10.1175/1520-0442(1998)011<0831:ADCCIT>2.0.CO;2.

Haak, H., J. Junglaus, U. Mikolajewicz, and M. Latif, 2003: Formation and propagation of great salinity anomalies. *Geophys. Res. Lett.,* **30,** 1473, doi:10.1029/2003GL017065.

Harris, F. J., 1978: On the use of windows for harmonic analysis with the discrete Fourier transform. *Proc. IEEE,* **66,** 51–83, doi:10.1109/PROC.1978.10837.

Hasselmann, K., 1976: Stochastic climate models. Part I: Theory. *Tellus,* **28,** 473–485, doi:10.1111/j.2153-3490.1976.tb00696.x.

Hirschi, J., and J. Marotzke, 2007: Reconstructing the meridional overturning circulation from boundary densities and the zonal wind stress. *J. Phys. Oceanogr.,* **37,** 743–763, doi:10.1175/JPO3019.1.

——, J. Baehr, J. Marotzke, J. Stark, S. Cunningham, and J.-O. Beismann, 2003: A monitoring design for the Atlantic meridional overturning circulation. *Geophys. Res. Lett.,* **30,** 1413, doi:10.1029/2002GL016776.

——, P. D. Killworth, and J. R. Blundell, 2007: Subannual, seasonal, and interannual variability of the North Atlantic meridional overturning circulation. *J. Phys. Oceanogr.,* **37,** 1246–1265, doi:10.1175/JPO3049.1.

Hodson, D. L. R., and R. T. Sutton, 2012: The impact of resolution on the adjustment and decadal variability of the Atlantic meridional overturning circulation in a coupled climate model. *Climate Dyn.,* **39,** 3057–3073, doi:10.1007/s00382-012-1309-0.

Jayne, S. R., and J. Marotzke, 2001: The dynamics of ocean heat transport variability. *Rev. Geophys.,* **39,** 385–411, doi:10.1029/2000RG000084.

Johnson, H. L., and D. P. Marshall, 2002: A theory for the surface Atlantic response to thermohaline variability. *J. Phys. Oceanogr.,* **32,** 1121–1132, doi:10.1175/1520-0485(2002)032<1121:ATFTSA>2.0.CO;2.

Kanzow, T., and Coauthors, 2010: Seasonal variability of the Atlantic meridional overturning circulation at 26.5°N. *J. Climate,* **23,** 5678–5698, doi:10.1175/2010JCLI3389.1.

Kawase, M., 1987: Establishment of deep ocean circulation driven by deep-water production. *J. Phys. Oceanogr.,* **17,** 2294–2317, doi:10.1175/1520-0485(1987)017<2294:EODOCD>2.0.CO;2.

Knight, J. R., R. J. Allan, C. K. Folland, M. Vellinga, and M. E. Mann, 2005: A signature of persistent natural thermohaline circulation cycles in observed climate. *Geophys. Res. Lett.,* **32,** L20708, doi:10.1029/2005GL024233.

Köhl, A., 2005: Anomalies of meridional overturning: Mechanisms in the North Atlantic. *J. Phys. Oceanogr.,* **35,** 1455–1472, doi:10.1175/JPO2767.1.

Lee, T., and J. Marotzke, 1998: Seasonal cycles of meridional overturning and heat transport of the Indian Ocean. *J. Phys. Oceanogr.,* **28,** 923–943, doi:10.1175/1520-0485(1998)028<0923:SCOMOA>2.0.CO;2.

Madec, G., P. Delecluse, M. Imbard, and C. Levy, 1998: OPA 8.1 ocean general circulation model reference manual. IPSL Notes du Pole de Modelisation 11, 91 pp. [Available online at http://www.nemo-ocean.eu/About-NEMO/Reference-manuals.]

Marotzke, J., and B. A. Klinger, 2000: The dynamics of equatorially asymmetric thermohaline circulations. *J. Phys. Oceanogr.,* **30,** 955–970, doi:10.1175/1520-0485(2000)030<0955:TDOEAT>2.0.CO;2.

——, R. Giering, K. Q. Zhang, D. Stammer, C. Hill, and T. Lee, 1999: Construction of the adjoint MIT ocean general circulation model and application to Atlantic heat transport sensitivity. *J. Geophys. Res.,* **104,** 29 529–29 547, doi:10.1029/1999JC900236.

Marshall, J., H. Johnson, and J. Goodman, 2001: A study of the interaction of the North Atlantic Oscillation with ocean circulation. *J. Climate,* **14,** 1399–1421, doi:10.1175/1520-0442(2001)014<1399:ASOTIO>2.0.CO;2.

Matei, D., J. Baehr, J. H. Jungclaus, H. Haak, W. A. Muller, and J. Marotzke, 2012: Multiyear prediction of monthly mean Atlantic meridional overturning circulation at 26.5°N. *Science,* **335,** 76–79, doi:10.1126/science.1210299.

McCarthy, G., and Coauthors, 2012: Observed interannual variability of the Atlantic meridional overturning circulation at 26.5°N. *Geophys. Res. Lett.,* **39,** L19609, doi:10.1029/2012GL052933.

Meehl, G. A., and Coauthors, 2009: Decadal prediction: Can it be skillful? *Bull. Amer. Meteor. Soc.,* **90,** 1467–1485, doi:10.1175/2009BAMS2778.1.

Metz, W., 1991: Optimal relationship of large-scale flow patterns and the barotropic feedback due to high-frequency eddies. *J. Atmos. Sci.,* **48,** 1141–1159, doi:10.1175/1520-0469(1991)048<1141:OROLSF>2.0.CO;2.

Mignot, J., and C. Frankignoul, 2005: The variability of the Atlantic meridional overturning circulation, the North Atlantic Oscillation, and the El Niño–Southern Oscillation in the Bergen Climate Model. *J. Climate,* **18,** 2361–2375, doi:10.1175/JCLI3405.1.

Ortega, P., E. Hawkins, and R. Sutton, 2011: Processes governing the predictability of the Atlantic meridional overturning circulation in a coupled GCM. *Climate Dyn.,* **37,** 1771–1782, doi:10.1007/s00382-011-1025-1.

Parzen, E., 1962: On the estimation of the probability density function and the mode. *Ann. Math. Stat.,* **33,** 1065–1076, doi:10.1214/aoms/1177704472.

Pedlosky, J., 1979: *Geophysical Fluid Dynamics.* Springer-Verlag, 624 pp.

Penduff, T., J. Le Sommer, B. Barnier, A. M. Treguier, J.-M. Molines, and G. Madec, 2007: Influence of numerical schemes on current-topography interactions in 1/4° global ocean simulations. *Ocean Sci.,* **3,** 509–524, doi:10.5194/os-3-509-2007.

Persechino, A., R. Marsh, B. Sinha, A. P. Megann, A. T. Blaker, and A. L. New, 2012: Decadal-timescale changes of the Atlantic overturning circulation and climate in a coupled climate model with a hybrid-coordinate ocean component. *Climate Dyn.,* **39,** 1021–1042, doi:10.1007/s00382-012-1432-y.

Pohlmann, H., D. M. Smith, M. A. Balmaseda, N. S. Keenlyside, S. Masina, D. Matei, W. A. Müller, and P. Rogel, 2013: Predictability of the mid-latitude Atlantic meridional overturning circulation in a multi-model system. *Climate Dyn.,* **41,** 775–785, doi:10.1007/s00382-013-1663-6.

Roberts, C. D., and Coauthors, 2013: Atmosphere drives recent interannual variability of the Atlantic meridional overturning circulation at 26.5°N. *Geophys. Res. Lett.,* **40,** 5164–5170, doi:10.1002/grl.50930.

Robson, J., R. Sutton, K. Lohmann, D. Smith, and M. D. Palmer, 2012: Causes of the rapid warming of the North Atlantic Ocean in the mid-1990s. *J. Climate,* **25,** 4116–4134, doi:10.1175/JCLI-D-11-00443.1.

——, ——, and D. Smith, 2013: Predictable climate impacts of the decadal changes in the ocean in the 1990s. *J. Climate,* **26,** 6329–6339, doi:10.1175/JCLI-D-12-00827.1.

Roullet, G., and G. Madec, 2000: Salt conservation, free surface, and varying levels: A new formulation for ocean general

circulation models. *J. Geophys. Res.,* **105,** 23 927–23 942, doi:10.1029/2000JC900089.

Sime, L. C., D. P. Stevens, K. J. Heywood, and K. I. C. Oliver, 2006: A decomposition of the Atlantic meridional overturning. *J. Phys. Oceanogr.,* **36,** 2253–2270, doi:10.1175/JPO2974.1.

Stepanov, V. N., and K. Haines, 2013: Mechanisms of AMOC variability simulated by the NEMO model. *Ocean Sci. Discuss.,* **10,** 619–648, doi:10.5194/osd-10-619-2013.

Sutton, R. T., and D. L. R. Hodson, 2007: Climate response to basin-scale warming and cooling of the North Atlantic Ocean. *J. Climate,* **20,** 891–907, doi:10.1175/JCLI4038.1.

——, and B. Dong, 2012: Atlantic Ocean influence on a shift in European climate in the 1990s. *Nat. Geosci.,* **5,** 788–792, doi:10.1038/ngeo1595.

Thomson, D. J., 1982: Spectrum estimation and harmonic analysis. *Proc. IEEE,* **70,** 1055–1096, doi:10.1109/PROC.1982.12433.

Timmermann, A., M. Latif, R. Voss, and A. Grötzner, 1998: Northern Hemispheric interdecadal variability: A coupled air–sea mode. *J. Climate,* **11,** 1906–1931, doi:10.1175/1520-0442-11.8.1906.

Uppala, S. M., and Coauthors, 2005: The ERA-40 Re-Analysis. *Quart. J. Roy. Meteor. Soc.,* **131,** 2961–3012, doi:10.1256/qj.04.176.

Yeager, S., and G. Danabasoglu, 2014: The origins of late-twentieth-century variations in the large-scale North Atlantic circulation. *J. Climate,* **27,** 3222–3247, doi:10.1175/JCLI-D-13-00125.1.

Zhang, R., 2008: Coherent surface-subsurface fingerprint of the Atlantic meridional overturning circulation. *Geophys. Res. Lett.,* **35,** L20705, doi:10.1029/2008GL035463.

——, 2010: Latitudinal dependence of Atlantic meridional overturning circulation (AMOC) variations. *Geophys. Res. Lett.,* **37,** L16703, doi:10.1029/2010GL044474.